TECHNISCHE
UNIVERSITÄT
WIEN
Vienna University of Technology

MASTER THESIS

3D-Reconstruction of the E3 Ligase LUBAC by Cryo-Electron microscopy

Author:
Filip STANISZEWSKI

Supervisor:
Prof.-Dr. David HASELBACH,
Univ. Prof. Dipl.-Ing. Dr.techn.
Gerhard SCHÜTZ

A thesis submitted in fulfilment of the requirements for the degree of Dipl. Ing.

in the

Biophysics Group
Institute of Applied Physics

July 26, 2022

TECHNISCHE
UNIVERSITÄT
WIEN
Vienna University of Technology

DIPLOMARBEIT

3D-Rekonstruktion der E3 Ligase LUBAC mittels Kryo-Elektronenmikroskopie

Autor:
Filip STANISZEWSKI

Betreuer:
Prof.-Dr. David HASELBACH,
Univ. Prof. Dipl.-Ing. Dr.techn.
Gerhard SCHÜTZ

Zur Erlangung des Grades Dipl. Ing.

Biophysik Gruppe
Institute für Angewandte Physik

26. Juli 2022

Declaration of Authorship

I, Filip STANISZEWSKI, declare that this thesis titled, "3D-Reconstruction of the E3 Ligase LUBAC by Cryo-Electron microscopy" and the work presented in it are my own. I confirm that:

- This work was done wholly or mainly while in candidature for a research degree at this University.
- Where any part of this thesis has previously been submitted for a degree or any other qualification at this University or any other institution, this has been clearly stated.
- Where I have consulted the published work of others, this is always clearly attributed.
- Where I have quoted from the work of others, the source is always given. With the exception of such quotations, this thesis is entirely my own work.
- I have acknowledged all main sources of help.
- Where the thesis is based on work done by myself jointly with others, I have made clear exactly what was done by others and what I have contributed myself.

Signed:

Date:

TECHNISCHE UNIVERSITÄT WIEN

Zusammenfassung

Biomedical Engineering
Institute für Angewandte Physik

Dipl. Ing.

3D-Rekonstruktion der E3 Ligase LUBAC mittels Kryo-Elektronenmikroskopie

von Filip STANISZEWSKI

Der *Lineare Ubiquitin Chain Assembly Complex* (LUBAC) ist die einzig bekannte Ubiquitin-Ligase, die lineare Ubiquitinketten generiert. In der Vergangenheit konnte gezeigt werden, dass LUBAC ein essentieller Agonist in der NF-κB Kaskade ist und somit in Entzündungsreaktionen und immunologischen Reaktionen involviert ist. LUBACs Untereinheiten konnten einzeln bereits rekonstruiert werden, jedoch ist es bislang nicht gelungen eine hoch aufgelöste 3D Struktur des vollständigen LUBAC zu erlangen. Diese Arbeit präsentiert sowohl ein optimiertes Verfahren um LUBAC mit hoher Reinheit und Integrität aufzureinigen, als auch eine 3D Rekonstruktion des Proteins. Es werden außerdem die Eigenschaften des LUBACs auf kryo-EM Probengittern unter verschiedenen Konditionen untersucht und analysiert. Dabei konnte gezeigt werden, dass die Adhäsion von LUBAC zur Wasseroberfläche für die Dissoziierung des Proteins verantwortlich ist und somit zu einer verminderten Auflösung in der Rekonstruktion führt. Die Immersion der Teilchen konnte mittels verschiedener Methoden verbessert werden. Die Totzeit zwischen dem Abtupfen des kryo-EM Gitters und dem Eintauchen in flüssiges Ethan muss stark reduziert werden um die Adhäsion von LUBAC Teilchen an die Wasseroberfläche zu verhindern.

VIENNA UNIVERSITY OF TECHNOLOGY

Abstract

Biomedical Engineering
Institute of Applied Physics

Dipl. Ing.

3D-Reconstruction of the E3 Ligase LUBAC by Cryo-Electron microscopy

by Filip STANISZEWSKI

The linear ubiquitin chain assembly complex (LUBAC) is the only known ubiquitin ligase for linear/M1-linked ubiquitin chain formation. It was shown that LUBAC is an essential agonist in the NF-κB pathway and thus involved in inflammation and immune signalling. Many structures of the subunits of LUBAC bound to other proteins have been reconstructed already; however, a high-resolution 3D reconstruction of the human LUBAC could not be achieved yet. This project presents an optimized purification procedure for LUBAC with very high purity and integrity, as well as a 3D reconstruction at low resolution. The exceptional behaviour of LUBAC on cryo-EM grids under various grid conditions and modifications was analysed and described. This thesis found that the adhesion of LUBAC to the air-water-interface on cryo-EM grids heavily reduces resolution, as it causes LUBAC to disassemble. Particle immersion into solution could be improved; however, not fully overcome. The delay time between blotting and plunge freezing needs to be drastically reduced, to inhibit the adsorption of LUBAC to the air-water interface.

Acknowledgements

I would like to thank the whole Haselbach lab, especially my supervisor, David Haselbach, who guided me through this thesis and whose expertise in Cryo-Electron microscopy was invaluable for the accomplishing many goals throughout this Project. Moreover, I want to thank Irina Grishkovskaya for the introduction to the wet lab and Zuzana Hodakova for scientific advice and guidance. I would also like to thank the members of the VBC core facilities for the introductions to the several devices, notably Thomas Heuser and Harald Kotisch from the EM facility. Furthermore, I would like to thank my assessor Gerhard Schütz from TU Vienna for, whose passion for biophysics inspired me for this project.

Contents

List of Figures

List of Tables

List of Abbreviations

Ub	Ubiquitin
E1,E2,E3	Enzyme 1, 2, 3
DNA	Desoxyribonucleic acid
ATP	Adenosintriphosphat
Cys	Cysteine
Lys	Lysine
Met	Methionine
HECT	Homologous to E6AP C-Terminus
RBR	RING in-between RING
UbCH5	Ubiquitin-conjugating Human 5 enyzme
UbCH7	Ubiquitin-conjugating Human 7 enyzme
LUBAC	Linear Ubiquitin assembly complex
HOIP	HOIL-1L interacting protein
HOIL-1L	RanBP-type and C3H4-type zinc finger containing protein
SHARPIN	Shank-associated RH domain- interacting protein
M1	Methionine 1
NF-kB	Nuclear factor κ-light-chain-enhancer of activated B-cells
TNFR	Tumor necrosis factor receptor
TLR	Toll-like receptors
IkBa	B-cell inhibitor alpha
IKK	IκB Kinase
NEMO	Nf-κB essential modulator
UBL	Ubiquitin-like domain
UBA	Ubiquitin associated domain
NZF	Zinc finger domain
LDD	Chain-determining domain
DUB	Deubiquitinase
OTULIN	OUT deubiquitinase with linear linkage specificity
CYLD	Carboxyl-terminal hydrolase
PUB	Peptide:N-glycanase/UBA or UBX-containing proteins
ORAS	Otulin-related autoinflammation syndrome
MP	Mass Photometry
IRM	Interference reflection microscopy
iSCAT	Scattering microscopy
TEM	Transmission electron microscopy
DDC	Direct detection camera
CTF	Contrast transfer function
SPA	Single particle analysis
SDS	Sodium dodecyl sulphate
GFP	Green Fluorescent protein
PCR	Polymerase chain reaction

SF9	Insect Cell line
BEVS	Baculovirus expression vector system
AC	Affinity Chromatography
SEC	Size Exclusion Chromatography
DSF	Differential scanning fluorimetry
PEI	Polycationic polymer
GO	Graphene Oxide
ET	Electron Tomography
crYOLO	Cryo-EM YOLO (you only look once)
cryoSPARC	Cryo-EM Single Particle Ab Initio Reconstruction and Classification

Chapter 1

Introduction

1.1 Ubiquitination

Post-translational modifications are essential for the maturity of protein products. These modifications of proteins enable and regulate cellular processes and physiological responses. Besides phosphorylation and acetylation, ubiquitination is one of the most common post-translational modifications [1]. Ubiquitination is characterized by covalent attachment of ubiquitin (Ub) to a target protein. Besides its flexible C-terminal tail, Ub is an 8 kDa small, highly compact globular protein [2]. Ubiquitination is a well-regulated process that involves three different enzymes (E) including the activating E1, conjugating E2, and ligating E3. While there are only two known E1s in the human genome, there are roughly 40 E2s and over 600 E3 enzymes [3]. This set of enzymes is responsible for regulating many processes within cells such as DNA repair, signalling and cell cycle control [4]–[6]. In the first step of the substrate ubiquitination cascade, ATP and ubiquitin bind the E1 to initiate adenylation of the C-terminus of Ub. In the next step the catalytic cysteine (Cys600) mediates the formation of a thioester bond between the E1 and Ub. A thioester transfer reaction is necessary to transfer the Ub from the E1 to the catalytic Cys residue of an E2. Most E2 Ub conjugates can pair with one or more E3 ligases, facilitating the Ub transfer onto the substrate's amino group. The Ub attachment to substrate occurs at the amino group of the substrate's lysine residue (Fig. 1.1) [7]. There are three known major types of E3 ligases: Really Interesting New Gene (RING)-type E3s, Homologous to E6AP C-terminus (HECT)-type E3s, and RING-in-between-RING (RBR) E3s. Depending on the E3 type, Ub can be transferred directly on the substrate (RING-type) or via an intermediate step, where the Ub is transferred to the catalytic Cys of the E3 (HECT type) [8]. The third class of E3 ligases (RBR type) were shown to function via a RING/HECT hybrid mechanism [9]. Like HECT-type E3s, the RBR-type E3s proceed through the recognition of E2 Ub conjugate by their first RING domain (RING1), and transfer the Ub to the catalytic cysteine on the second RING domain (RING2) to form a thioester intermediate. Finally, RING2 transfers the Ub to the substrate and monoubiquitinates it [10]. The substrate can either stay in a mono-ubiquitin modification or be further modified by the attachment of Ub-chains. In the latter case a second (or more) Ub will be attached to the C terminus of the first Ub. The chain type depends on where the second Ub binds. Any of the eight amino groups (Met1, Lys6, Lys11, Lys27, Lys29, Lys33, Lys48, Lys63) of the subsequent Ubs can act as a binding site. However, this process is also dependent on the E3 ligase and conjugating E2 that contribute to the process of ubiquitination of the substrate. Each E3-E2 pair generates specific Ub-chains [11], [12]. Homotypic chains are chains where the Ub are connected via one specific linkage type (e.g. Lys48). But chains can also be heterotypic, with more than one linkage type is present. In this case it is also possible that branched poly-Ub chains are generated as more than one binding site per Ub is available for linkage. It is hypothesised that linkage types may trigger different biological responses [13]. For example,

Lys48 linked Ub-chains have been shown to be an essential agonist in proteasomal degradation [14]. There are many more linkage types and functions, however, the complexity of ubiquitin-dependent signaling remains poorly understood [15], [16].

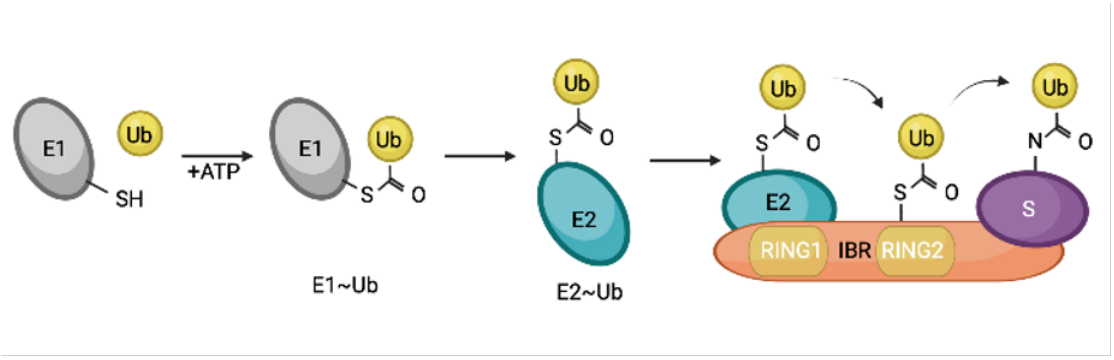

FIGURE 1.1: Ubiqutination Cascade. 1 ATP is required to attach Ub to the E1. Ub then gets transferred to the E2, which binds the RING1 domain of the E3, subsequently. The Ub is moved to the RING2 domain by transthiolation and finally the substrate gets ubiquitinated

Both UbCH5 and UbCH7 are conjugating E2s and are associated with LUBAC. All E2 proteins share a topologically conserved α/β -fold core domain (UBC core, responsible for the recognition of E1s and the transfer of Ub to E3s. Some E2 possess N- or C-terminal extensions that add additional functionality. UbCH5b and UbCH7 were both shown to transfer ubiquitin to the E3 Linear Ubiquitin Assembly Complex (LUBAC) [17]. Furthermore, UbCH5b was also found to bind the RBR-domain of HOIP [18].

1.2 The NF-κB Pathway and LUBAC

M1-linked Ub-chains play an elementary role in the initiation of the *Nuclear Factor κ-light-chain-enhancer of activated B-cells* (NF-κB). As the linear ubiquitin assembly complex, LUBAC, is the only known E3 ligase to generate linear chains. Its most prominent function involves the activation of the NF-κB pathway. Nuclear factor - κB represents a family of inducible transcription factors, which's activations plays a crucial role in inflammation and immune response. There are two signalling pathways related to NF-κB, the canonical and the alternative pathway. The canonical pathway can be activated by stimuli from cytokine receptors, tumor necrosis factor receptors (TNFR), toll-like receptors (TLR), T-cell as well as B-cell receptors [19]–[21]. Although the pathway differs in the use of ligands and proteins depending on which receptor is activated, the general mechanism of induced degradation of nuclear factor of κ light polypeptide gene enhancer in B-cells inhibitor alpha (IκBα) is shared by all of them. IκBα inhibits NF-κB by masking nuclear localization signals necessary for the import into nuclei [22]. Therefore, IκBα needs to be removed from NF-κB so the pathway can be activated. The degradation of IκBα is achieved by phosphorylation by the IκB kinase (IKK) complex, which consists of three subunits, IKKa, IKKb, and the regulatory NF-κB essential modulator (NEMO). The phosphorylation of IKK triggers the ubiquitin-dependent IκB degradation by the proteasome, effectively enabling NF-κB members to be translocated to the nuclei rapidly and without any hindrance (Fig. 1.2 [23]. It was shown that the linear ubiquitination of NEMO by LUBAC is required for efficient NF-B activation induced by TNFa [24]. The ubiquitination of NEMO causes the activation of the IKK complex, which effectively leads to the phosphorylation

of the IκBα. Once NF-κB is imported to the nucleus, the transcription of inflammation-associated genes is facilitated, these include Cyclooxygenase-2 and Interleukin-6 for example [25], [26]. As LUBAC is thus far the only known E3 that generates M1-linked linear ubiquitin chains, it raises two questions: How does the LUBAC machinery generate linear Ub-chains, and what essential functions does it fulfil in cells? A high resolution 3D strucutre is necessary. So far, it was shown that LUBAC is an assembly of three proteins in a 1:1:1 stoichiometry: RanBP- type and C3H4-type zinc finger containing protein (HOIL-1L), HOIL-1L interacting protein (HOIP) and shank-associated RH domain- interacting protein (SHARPIN), which have masses of 120, 59 and 43 kDa, respectively. LUBAC thus has a total molecular weight of 222 kDa but can also form a 444 kDa homodimeric complex [24], [27]. The ubiquitin-like domains (UBL) of HOIL-1L and SHARPIN have been shown to bind to HOIP via its ubiquitin-associated domain (UBA)(Fig. 1.2) [28]. Additionally, the zinc finger domain (NZF2) of HOIP binds to the UBL domain of SHARPIN [29]. However the precise contacts unknown as there is only crosslinking data and a low-resolution structure are available for LUBAC [27]. Although, a high-resolution structure of LUBAC that displays the binding sites and assembly of the subunits is still missing, recent publications partially explained the LUBAC-linear-Ub machinery and its characteristics. However, a detailed and complete understanding has yet to be found.

One unique characteristic of LUBAC is that it consists of two catalytically active RBR-E3 ligases: HOIP and HOIL-1L. While HOIP has been shown to generate M1-linked Ub chains, HOIL-1L catalyzes the monoubiquitylation of proteins in cells [30]. Interestingly, HOIL-1L is an atypical E3 ligase as it forms oxyester bonds between the C-terminal carboxylate of Ub and serine and threonine residues in its substrates [30]. The catalytic activity of LUBAC is provided by the RBR-domains of HOIP and HOIL-1L, as well as the chain-determining domain (LDD) of HOIP [31]. Although, HOIL-1L and SHARPIN alone cannot generate linear Ub chains, it was shown that in complex with HOIP, they contribute to the forming these Ub chains [17]. LUBAC and linear Ub-chains are heavily involved in the activating the NF-κB pathway and, therefore, inflammation and immune signalling. Dysfunctional LUBAC results in deregulation of the M1-linked ubiquitin machinery. Mutations in the HOIL-1L interacting protein (HOIP) encoding gene RNF31 and RanBP- type and C3H4-type zinc finger containing protein (HOlL-1L) showed multi-organ auto-inflammation and immunodeficiency in vivo [32], [33]. However, LUBAC is not the only protein that mediates NF-kB activation. The regulation of linear Ub chains is also controlled by deubiquitinases (DUBs) such as Ubiquitin thioesterase otulin (OTULIN) and Ubiquitin carboxyl-terminal hydrolase CYLD (CYLD). Both complexes have been shown to bind the PUB domain of HOIP [34]. However, the proof of direct binding of OTULIN and the fully assembled LUBAC has not been shown yet [35]. Overexpression of OTULIN delays LUBAC-mediated NF-κB signalling upon TNF activation [36]. Conversely, OTULIN deficiency results in the accumulation of M1-linked Ub chains and uncontrolled inflammation, OTULIN-related Autoinflammation syndrome (ORAS) [37]. Thus, a balanced interaction of LUBAC with its DUBs, especially OTULIN, is an essential property of a healthy cell.

In conclusion, LUBAC is a key protein in the NF-κB pathway and M1-linked Ub chain generation. Due to its involvement in immune signalling and inflammation, it is an interesting protein regarding molecular pathology and, potentially, drug design.

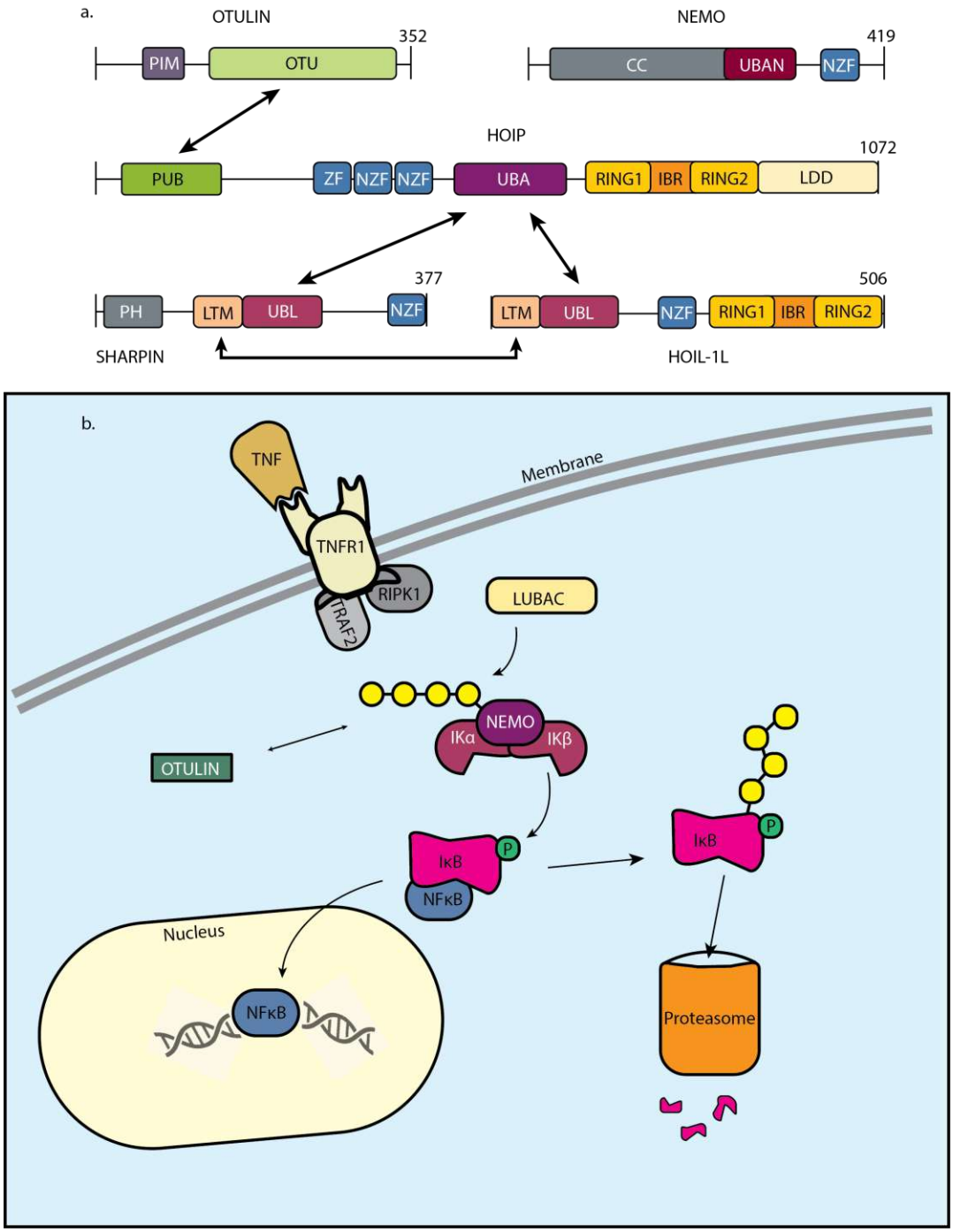

FIGURE 1.2: LUBAC and the NF-κB pathway. (a) OTULIN, NEMO, and the three subunits of LUBAC. Interacting domains are marked with arrows. (b) Simplified scheme of the NF-κB cascade

1.3 Mass Photometry

Mass Photometry (MP) is a technique which allows for precise and accurate quantification of the abundance of proteins according to their mass in a sample of interest. The method exploits two principles: interference reflection microscopy (IRM) and scattering microscopy (iSCAT). MP is a great addition to size exclusion chromatography and density gradients as it allows to survey the heterogeneity of the sample by requiring only very little sample (1 to 2 μL at mM is sufficient for a series of measurements). Fundamentally, an MP device measures the relative contrast of particles against the background caused by the reflection and scattering of the incident light beam (laser). The measured intensity at the detector is a superposition of the scattered and refracted light and is equal to

$$I_d = |E_r + E_s|^2 = E_i^2[r^2 + s^2 + 2r|s|cos(\phi)] \tag{1.1}$$

E_r: is the electric field of the reflected ray

E_s: is the electric field of the scattered ray

E_i: is the electric field of the incident ray

r: is the cross-section of the reflected ray

s: is the cross-section of the scattered ray

ϕ: phase difference of E_r and E_s

The refractivity of a surface can be estimated by the Fresnel equation (for an incident light angle of 0°) [38]:

$$r = \frac{n_2 - n_1}{n_2 + n_1} \tag{1.2}$$

n_2: refractive index of the medium

n_1: refractive index of the coverslip

In MP, the contribution of the reflected light, which is the r^2 term, dominates the light intensity at the detector. Therefore, the scattering term s^2 can be excluded from equation (1.1). Furthermore, the interferometric term will become significant in the case of long coherence length of the incident light beam, which is true in the case of laser light. In MP measurements the reflected light can be considered as the reference signal against which the intensity due to interference of scattered with reflected light is being measured. The amount of scattered light is proportional to the scattering cross section (σ), which is

$$\sigma = |s|^2 = \frac{\epsilon_m^2 \pi D^6}{4\lambda^4} \left| \frac{\epsilon_p(\lambda) - \epsilon_m(\lambda)}{\epsilon_p(\lambda) + 2\epsilon_m(\lambda)} \right| \tag{1.3}$$

ϵ_m: dielectric constant of the medium

ϵ_p: dielectric constant of the particle

λ: wavelength

D: particle diameter

Thus, the intensity at the light detector is proportional to D^3, [39] and the relative contrast values obtained from the MP measurement are proportional to the mass of the macromolecules (Fig. 1.3). A set of pre-analysed proteins (usually a in the range of 50 – 1000 kDa) with known mass can be used to calibrate contrast-levels according to their masses.

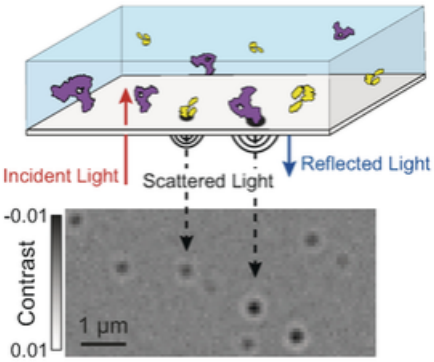

FIGURE 1.3: Principle of Mass Photometry. Bigger particles will display higher contrast during the measurement because the amount of scattered light is proportional to the diameter^3 of the particle. [40]

1.4 Cryo-Electron microscopy

Transmission electron microscopy (TEM) is a potent method to analyse samples with appropriate thickness. Specifically, cryo-EM can resolve structures of biological macromolecules such as proteins, as well as, organelles in near-native states to high resolution [41]. Depending on the integrity and homogeneity of the studied protein, it is possible to resolve structures from several angstroms up to the atomic resolution, as it was shown for the highly symmetric protein apoferritin [42]. Since the first biological structure was obtained by TEM in 1984 by Dubochet's group, an increasing number of proteins have been examined with cryo-EM [43]. Before the cryo-EM "resolution revolution", which involved the introduction of new direct electron detectors significantly enhancing the achievable resolution, crystallography used to be the conventional method for structural biology and remains an important technique in this field. However, the drawbacks are apparent. Crystallization requires large amounts of purified proteins (up to 10 times more than cryo-EM). In some cases, chemical modification of macromolecules is necessary for crystallization, and proteins are not in their native state. In cryo-EM, the proteins can be kept in buffers which resemble physiological conditions. Especially for disordered flexible proteins crystallization is not suitable, as these do not form crystals readily. On the other hand, cryo-EM allows visualising these, albeit not to high resolution either. It can, in certain cases, provide a low-resolution 3D envelope of the whole protein, including its disordered and flexible regions. [44], [45]. LUBAC and E3 ligases in general are likely to have flexibility issues too. While an 8 diffraction pattern from a crystal is not sufficient to build any kind of model, a 8 cryo-EM volume could give an idea of what the true structure might look like. In TEM, very thin samples are irradiated with highly accelerated electrons that are emitted from an electron emission source (cathode, gun). The main advantage of electron microscopy compared to conventional light microscopy is the theoretical maximum resolution. The Abbe limit states that the maximum resolution for light microscopes is

$$d = \frac{\lambda}{2NA} \tag{1.4}$$

d: minimal distance to be resolved

λ: wavelength

NA: numerical aperture

As light microscopy uses light (λ = 300 -700 nm), the resolution is limited. In comparison, in cryo-EM, there is no theoretical limit as the electron wavelength can become arbitrarily large if the accelerating voltage can be increased. The wavelength of electrons can be calculated with the de Broglies equation:

$$\lambda_e = \frac{h}{\sqrt{2m_0E(1 + \frac{E}{2m_0c^2})}} \tag{1.5}$$

λ_e: wavelength electron

h: Planck constant

m_0: electron mass

E: Energy of electron

c: speed of light constant

Although there is no theoretical limit, the resolution is practically limited to 0.1 nm due to the objective lens system and aberrations in electron microscopes. A TEM consists of five major components: an electron source (gun), electron lens system, apertures, specimen, and a detector. Electrons are emitted by field electron emission and thermionic emission by applying a high voltage source to the gun (100 – 300 kV). Electromagnets are used to generate a magnetic field in the TEM that can focus electrons. Annular metallic plates serve as apertures to exclude electrons that are further away from the optical axis, as they are more likely caused by spherical and chromatic aberrations. In TEM, specimens will absorb and scatter electrons and cause phase shifts in the electron's wavefunction. Together these effects produce the observed image, which in newer TEM is recorded with a direct-detection camera (DDC). However, phase contrast is very small for soft-matter samples with low atomic number elements as they cause only small-angle scattering. Phase contrast can be increased by underfocusing, at the cost of blurring the image. Going out of focus shifts phases of scattered electrons increasingly with rising frequency. Therefore, the interference becomes frequency-dependent, and the contrast becomes dependent on defocus [46]. The contrast transfer function (CTF) describes this dependency.

1.5 Grid Preparation in Cryo-Electron microscopy

A very important advantage of cryo-EM is that proteins remain in a near-native state. The fixation of macromolecules relies on freezing a thin sample-buffer film on a grid support, such as copper mesh coated with a holey carbon film [47]. As the crystallization of water molecules in the buffer would reduce the structural integrity of the proteins, the grid is frozen rapidly by plunging it into liquid ethane. The quick cooling ensures that the solvent remains in an amorphous and non-crystalline state [48]. Another method that does

not require rapid vitrification is negative stain microscopy. The particles are embedded into a heavy element solution (e.g. uranyl acetate), that surrounds the particle and will absorb much more electrons in TEM than the protein itself. The contrast is enhanced as the proteins appear bright on a dark background (hence the name negative stain). The resolution obtained from negative stain is usually lower than in cryo-EM. However, it is suited for quick and preliminary experiments to analyse particle composition [49].

1.6 Image Processing

A crucial step in SPA is processing of particle images and 3D reconstruction of the protein of interest. As datasets contain up to millions of particle images with different orientations and often many conformations, processing is a computationally challenging task. Over the years, different approaches have been proposed to overcome these hurdles, namely Sparx, cryoSPARC and Relion to name a few [50]–[52]. Fundamentally, these algorithms make use of a Bayesian likelihood framework

$$\arg\max_{V_{1\ldots k}} logp(V_{1\ldots k}|X_{1\ldots k}) = \arg\max_{V_{1\ldots k}} logp(X_{1\ldots k}|V_{1\ldots k}) + logp(V_{1\ldots k}) = \arg\max f(V) \quad (1.6)$$

V_i: 3D structures that best describe observed images X_i

$f(V)$: objective function

X_i: observed images

The governing question asked here is: What is/are the most likely structure/s ($V_{1\ldots k}$) considering this set ($X_{1\ldots k}$) of images? Setting the partial derivative ($\frac{\partial f(V)}{\partial V_k} = 0$) and finding its maximum would give the best 3D structure that describes a given data collection. However, this step requires the integration of the probability density function over all possible poses of the obtained images. As this would require enormous computational power, the gradient is calculated for a batch of images. The 3D structure is then updated in the direction of the gradient according to the equation

$$dV_k = C_{men} dV_k^{n-1} + (1 + C_{mem})\eta_k \frac{\partial f(V)}{\partial V_k} \quad (1.7)$$

dV_k: 3D structure update

C_{mem}: "Memory" term

$dV_k^{(n-1)}$: previous structure update

Where the second term accounts for corrections due to the gradient descent with the rate constant η, while the first part serves as a "memory" term, which effectively reduces the corrections as the 3D structure converges towards the true structure. This method is also known as stochastic gradient descent (SGD) [51].

1.7 Problem Statement

LUBAC is the only known E3 ligase able to form linear M1-linked ubiquitin chains. It is a crucial component of the NF-κB pathway, necessary for numerous immune responses. It was shown that there are several substrates as well as deubiquitinases that interact with

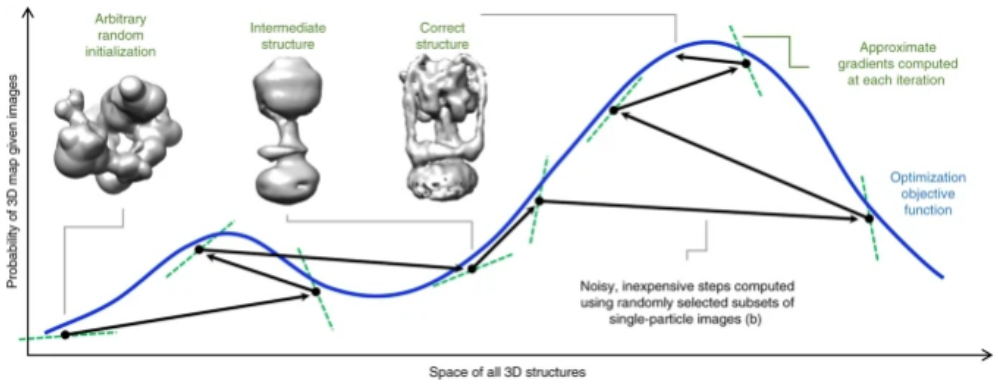

FIGURE 1.4: Stochastic Gradient Descent (SGD). On the left end side the volume is arbitrarily initialized. In each iteration of the algorithm the gradient of the objective function is calculated for a subset of images. Coming closer to the true model of the structure, the batch size increases, and the step-size becomes smaller to ensure convergence. Illustration taken from [51]

LUBAC. In recent years, many papers on the biochemical properties and biological function of LUBAC have been published. However, a high-resolution structure is necessary to understand the fundamental mechanism that governs the generation of linear ubiquitin chains and the assembly of LUBAC. Although work by Carvajal et al. leads to obtaining a low-resolution envelope of LUBAC, it is not sufficient to interpret LUBAC's mode of action. This work will attempt to obtain a high-resolution structure of LUBAC by SPA in cryo-EM. LUBAC will be purified, and the heterogeneity and structural integrity of the sample will be analysed by various techniques to validate the integrity and homogeneity of the sample. The long-term goal of this project is to understand the involvement of individual LUBAC subunits in generating the M1 ubiquitin chains from a molecular perspective and thus bring new insight into immune signalling by activating the NF-κB pathway.

Chapter 2

Materials and Methods

2.1 Materials

Chemical	Source
Dithiothreitol (DTT)	Carl Roth
Kanamycin (Km)	Sigma Aldrich
Magnesium chloride	Sigma Aldrich
Magnesium Sulphate	Sigma Aldrich
NP-40	Calbiochem
Potassium chloride	Sigma Aldrich
Sodium chloride	Sigma Aldrich
Sodium dodecyl sulphate (SDS)	Sigma Aldrich
Sterile Mono Q	MolBio Service, IMP
PageRuler TM Unstained Protein Ladder, 10 to 250 kDa	Thermo Scientific
PageRuler TM Prestained Protein Ladder, 10 to 250 kDa	Thermo scientific
D-Desthiobiotin	Sigma Aldrich
PEI (40k MW)	
GO	Sigma Aldrich
TCEP	Sigma Aldrich
Precision Plus Protein TM Unstained Protein Standards Marker	Bio-Rad
Phusion® High-Fidelity PCR Master Mix	Thermo Fisher

Enzymes	Source
5000x Benzonase	MolBio Service, IMP
GST-3c Precission protease	MolBio Service, IMP

Detergent	Source
β-D-Glucoside	Sigma Aldrich
DTT	Thermo Fisher
CTAB	Sigma Aldrich
LMNG	Thermo Fisher
CHAPSO	Merck

Buffer and Media	Composition
1x SDS running buffer	3% (w/v) Tris, 1.44% (w/v) glycine, 0.1% (w/v) SDS
1 x PBS buffer	137mM NaCl, 2.7 mM KCl, 10mM Na2HPO4, 1.8 mM KH2PO4
Lysis Buffer	50mM HEPES pH 8.0, 300mM NaCl, 0,5mM TCEP
Gel Filtration (GF-) Buffer	50mM HEPES pH 8.0, 150mM NaCl, 0,5mM TCEP
Elution Buffer	50mM HEPES pH 8.0, 150mM NaCl, 0,5mM TCEP, 5mM Desthiobiotin
Bicine Buffer	50mM Bicine pH 9, 150mM NaCl, 0,5mM TCEP
ZY Medium Autoinduction Medium	1% (w/v) tryptone, 0.5% (w/v) yeast extract, 25 mM (NH4)2SO4, 50 mM KH2PO4, 50 mM Na2HPO4, 0.5% v/v glycerol, 0.05% w/v glucose, 0.2% w/v alpha-lactose, 1 mM MgSO4
LB Medium	1% (w/v) tryptone, 0.5% (w/v) yeast extract, 1% (w/v) NaCl
SOC Medium	2% (w/v) tryptone, 0.5% (w/v) yeast extract, 10 mM NaCl, 2.5 mM KCl, 10 mM MgCl2, 10 mM MgSo4, 20 mM glucose

Equipment	Manufacturer
Amicon R Ultra Centrifugal Filter	Sigma Aldrich
AEKTA Pure	Cytiva
NGS Quest 100 Bio-Rad Chromatography System	BioRad
ChemiDoc MP Imaging System	Bio-Rad
Eppendorf TM 5424 Microcentrifuge	Eppendorf
Glacios Cryo-TEM	Thermo Fisher
Leica EM GPP	Leica
Quantifoil R 1.2/1.3 Cu200 holey carbon	Quantifoil
Tecnai G2 20	Thermo Fisher
Titan/Krios Cryo-TEM	Thermo Fisher
Whatman R qualitative filter paper, Grade 1	Sigma Aldrich
ThermoMixer C	Eppendorf
Zeba TM spin desalting Column, 7K MWCO, 0.5mL	Thermo Fisher
Ultracentrifuge XE600	Beckmann Coulter
Rotor SW 60 Ti (4ml tubes)	Beckmann Coulter
C1000 Series Touch Thermal Cycler	Biocompare

Column	Manufacturer
HiLoad R Superdex R 200pg 10/300 24mL	Cytiva
StrepTrap TM 5mL	Cytiva
HisTrap TM 5mL	Cytiva
StrepTrap R HP 1 mL	Cytiva

TABLE 2.1: Materials

2.2 SDS-PAGE

Sodium dodecyl sulphate polyacrylamide gel electrophoresis (SDS-PAGE) is an analytical method in biochemistry where individual proteins from a sample are separated in an electrical field according to their mass. The detergent SDS, together with high heat, denaturate and unfold the protein. On average, about two SDS molecules bind one amino acid, resulting in a constant charge distribution. The Separation of individual proteins is achieved by forcing them to move through a porous polyacrylamide gel by applying an electrical field. The negatively charged proteins move towards the anode, whereby proteins with higher molecular mass move slower through the gel [14]. In this thesis, Bio-Rad Criterion TM TGX Stain-FreeTM Precast Gels with acrylamide gradients from 4-15% and 4-20% were used. For all gels, 4μl of SDS was mixed with 8μl of sample, although only 6-8μl was loaded for samples obtained from pellets (P), flow-through (FT) and combined fractions (Comb). As a molecular weight standard, Precision Plus Protein TM Unstained Protein Standards Marker (Bio-Rad #1610363) was used. Gels were run at 200 V and 400 mA for 30-40 minutes at room temperature. Imaging was conducted on Bio-Rad ChemiDoc^{TM} Imaging Systems. If the signal was low, gels were additionally incubated in Coomassie stain for 1h at room temperature and imaged again.

2.3 PCR and Gibson Assembly of GFP-NEMO

Polymerase-Chain-Reaction (PCR) is used to amplify DNA sequences. The PCR can be described in 3 phases:

1. Denaturation: The DNA is heated to 95°C, which causes hydrogen bonds to break. Effectively, the DNA and primers are separated into single strands
2. Annealing: In a second step, the temperature is decreased to allow primer annealing to the single strand DNA. The annealing temperature is primer dependent and is chosen for ideal binding conditions for the primer to bind the desired locus.
3. Elongation: The temperature is increased again, and a polymerase generates the complementary strand. The whole cycle is then repeated several times to ensure sufficient amplification of the DNA

Once the DNA was amplified, the Vector and the Insert DNA needed to be connected, so the protein could be expressed in E. coli. The Gibson Assembly is a cloning method that links two linearised DNA with overlapping sequences: the Vector DNA and the Insert DNA. A 5' exonuclease is used to generate overhangs of the Insert and the Vector by digesting 5' DNA so that two DNA molecules can anneal. Then, a DNA polymerase fills the gaps [53]. In this thesis, NEMO was cloned into the vector pETM-33_ccdB for protein expression in E. coli. Forward and Reverse primers were designed and the coding sequence of NEMO, excluding the start codon, was copied into the ORF of pETM33,

downstream of a GFP site and a 3C cleavage site and upstream of the selection site ccdB. The forward primer (NEMO_FW) was defined as the 24 nucleotides of pETM33's 3C cleavage region and the first 27 nucleotides of the NEMO coding region. The reverse primer (NEMO_REV) was defined as the first 24 nucleotides of the ccdB sequence and the last 27 nucleotides of the NEMO coding region in reverse complement orientation. Primers were ordered from AddGene diluted with ddH2O ad 100 M each. PCR reactions were prepared using 50 ng template, 1 μM of primers NEMO_FW and NEMO_REV, 25 μL of 2x Phusion R High-Fidelity PCR Master Mix and 50 μL of ddH2O. The reaction was performed on a C1000 Series Touch Thermal Cycler (Biocompare) using 30 sec of initial denaturation at 95°C, 25 cycles of 15 sec denaturation at 95°C, 15 sec of annealing at 65°C and 15 sec elongation at 72°C, followed by 10 min of a final elongation step at 72°C. 5 μL of the PCR products were analysed on a 1% (w/v) Agarose gel containing Sybr Safe. PCR reactions containing NEMO DNA were purified by following the MiniPrep Protocol. Finally, for the Gibson Assembly, 70 ng of the Vector was combined with 10 times molar excess of Insert, 10 μL of 2 x Gibson Master Mix (Molecular Biology Service, IMP), and ddH2O ad 20 μL. The reaction was incubated for 1 h at 50°C on an Eppendorf Thermomixer without agitation. DNA from the Gibson reaction was transformed into E. coli DH5α after digestion with Dpn1 for 1 hour at 37°C and plasmid MiniPreps were performed on several colonies, as described previously. All the isolated plasmids were submitted for Sanger sequencing (Molecular Biology Service, IMP) using T7 forward and reverse primers. Therefore, samples covered the whole insert sequence (GFP-TEV-NEMO). Once the validity of the sequences was confirmed, they were used for expression in E. coli. OTULIN construct was kindly gifted from David Komander (full-length, aa 1-352, Addgene plasmid 61464 ; http://n2t.net/addgene:61464 ; RRID:Addgene_61464)

2.4 PCR Product Purification

250 μL binding buffer B was added to each PCR reaction, applied to a spin column in a fresh Eppendorf tube and centrifuged for 1 minute at 10,000 x g and 4°C. The flow-through was discarded, 750 μL washing Buffer W was added and centrifuged twice for 1 min at 10,000 x g and 4°C. The spin column was placed in a fresh Eppendorf tube, 50 μL of ddH2O was added, incubated for 1 min and centrifuged for 1 min at 10,000 x g and 4°C. Thereupon, the eluted DNA was quantified on a DeNovix DS-11 FX using the dsDNA quantification app.

2.5 Transformation of NEMO-GFP and OTULIN

Besides Transduction and Conjugation, Transformation is one of the 3 possible processes to transfer genes from one prokaryote to another [54]. *E. coli* cells must be competent to be able to incorporate the Vector-DNA. To facilitate this incorporation, *E. coli* cells are heat shocked after they have been mixed with the Vector-DNA. The heat shock will permeabilize the membrane for the vector DNA. Once the Vector-DNA has entered the cells, it is important to remove cells that do not contain the Insert DNA. Selection based on antibiotic resistance marker the vector carries a resistance gene for a certain antibiotic. By applying antibiotic treatment, only cells transformed with the vector carrying the resistance gene will survive. Large-scale expression is a procedure where the cells are grown in higher amounts so that larger amounts of protein can be harvested and purified [55]. Often the T7 expression system is used to achieve high overexpression of the protein of interest. In this system, the T7 polymerase is used to amplify the protein of interest, specifically by incorporating the T7 promoter in the transformed vector. The *E. coli* cell contains a gene that

can express and produce T7 polymerase, although it is controlled by a lac repressor. To prevent the inhibitory effect of the lac repressor, autoinduction media containing lactose is used to bind the lac repressor and prevent it from inhibiting gene expression. Effectively, once T7 polymerase transcription is activated by autoinduction, overexpression of the protein of interest is achieved rapidly [56] and can be used for purification. In this thesis, 5 μl of Plasmid DNA was mixed into 50 μl of competent cells (DH5α) and incubated on ice for 30 min. Then cells were heat-shocked for 1min at 42°CC and 800 rpm on a Thermomix (Eppendorf C), put back on ice and 250μl of SOC media. Competent cells were incubated for 1 hour at 37°CC and 750 rpm. Subsequently, 100μl of competent cells were put on Amp LB plates and incubated overnight at 37°C. Single colonies were picked the next day and inoculated in 5 ml of LB medium with appropriate antibiotics (concentration of 0.1 mg/ml, Ampicillin for NEMO, 0.5 mg/ml Kanamycin for OTULIN). Once again competent cells were incubated overnight at 37°C and 200 rpm. On the next day, cells were pelleted by centrifuging at 5000g for 10 min, and plasmids were isolated by following the Miniprep protocol. For the large-scale expression a few colonies from agar plates were picked, inoculated in 25 ml LB medium (also 0.1 mg/ml antibiotic concentration), and incubated overnight at 37°C and 300 rpm. The overnight culture was then inoculated in 6 L of ZY medium (see materials list). Large scale expression was then incubated at 37°C and 180 rpm for 5.5 hours before decreasing the temperature to 18°C for overnight incubation. On the next day, large-scale expression was centrifuged at 4000 rpm at 4°C and cell pellets were stored at -80°C.

2.6 Bacmid-prep and Insect cell culture

Although post-translation modifications (PTM) exist in prokaryotes, they are not as common and complex as in eukaryotes. As some proteins simply will not express in E. coli, eucaryotic systems are needed that allow for sufficient PTMs. Baculovirus expression vector systems (BEVS) are incorporated into standard methods in biology and used to amplify recombinant proteins in insect cells, e.g., Sf9. Baculoviruses offer advantages over other systems since they are nonpathogenic for mammals and easy to scale up. In BEVS, the polyhedrin gene is replaced with a recombinant gene that expresses the protein of interest. The polyhedrin gene has a high transcription rate resulting in a highly facilitated amplification of recombinant proteins. For this, the viral DNA is isolated from bacterial cells by using a miniprep system. Then the DNA can be transfected into insect cells by electroporation, for example, a technique in which an electrical field is applied to insect cells to increase the permeability of their cell membrane. Another technique uses lipids (such as Lipofectamine 2000) that form complexes with the viral-RNA and help them to overcome the electrostatic repulsion of the cell membrane [57]. In a virus plaque assay, the infectious potency of a virus can be estimated by observing the formation of plaque, which is purified subsequently. In this thesis, baculoviruses containing various derivatives of LUBAC were prepared by the in-house cell culture facility following a standard protocol as described roughly in the paragraph above. The transfer vector carrying the HsHOIP, His6-HsHOIL-1L, and Strep(II)-HsSHARPIN coding sequences were cloned using the GoldenBac cloning system [58] and transposed into the bacmid backbone carried by DH10EmBacY cells (Geneva Biotech). A V0 virus stock was generated from the bacmid in SF9 cells by transfecting with Lipofectamine 2000. V0 was amplified, and the new virus stock (V1) was used to infect 2-3 L cultures of SF9 cells (Expression Systems). Cells were grown in ESF 921 Insect Cell Culture Medium Protein Free (Expression Systems 96-001-01) at 27°C and infected at a density of 1x10^6 cells/ml. Cells were harvested 72 hours

after infection (infection rate > 80%, viability > 90%) by centrifuging at 1.800 g for 15 minutes, resuspension in 1x PBS, again centrifuging for 15 min, finally flash-frozen in liquid nitrogen and stored at -80°C.

2.7 Purification of recombinant LUBAC DCD from insect cells

The general purification pipeline included lysis of the cells followed by chromatography techniques. Cells were resuspended in Lysis Buffer (50 mM HEPES, 300 mM NaCl and 0.5mM TCEP, pH 8.0) supplemented with 1 tablet of cOmplete Mini EDTA-free protease inhibitor cocktail (Merk) and 100 mM Benzonase. Cells were lysed by four passes through a Constant Systems Cell Disruptor at 1.4 kBar. Lysates were cleared by centrifugation at 48,284 g for 45 min at 4°C and loaded onto a StrepTrap 5 ml (GE Healthcare). Complexes were concentrated using a Centriprep (Merck 4311) centrifugal filter with a 30 kDa cut-off, then flash-frozen in liquid nitrogen and stored at -80°

2.8 Affinity Chromatography

Affinity Chromatography (AC) is based on the highly specific binding of tagged proteins to biomolecules embedded in a stationary phase (matrix/resin). In this thesis, SHARPIN was N-terminally modified with a Strep-Tag, a sequence of 8 amino acids. Once the cell lysate is applied to the pre-equilibrated column, proteins with the Strep-Tag bind the streptavidin that is engineered into the column matrix. While tagged proteins (and proteins that are bound to it, e.g. HOIL-1L and HOIP) attach to the resin, untagged proteins flow through the column. In the final step, the bound proteins are eluted using low amounts of Desthiobiotin, an biotin analogue. Desthiobiotin competes with the protein for the Strep binding sites, resulting in the dissociation of the protein from the matrix [59]. Samples in this thesis were loaded on a StrepTrap 5ml (GE Healthcare), which was equilibrated with Lysis Buffer (50mM HEPES pH 8.0, 300mM NaCl, 0,5mM TCEP) and washed with GF-buffer (50mM HEPES pH 8.0, 150mM NaCl, 0,5mM TCEP). The washing step was conducted by applying 5 CV of GF-Buffer. Proteins were eluted with Elution-buffer (50 mM HEPES pH 8.0, 150 mM NaCl, 0.5mM and 5 mM D-desthiobiotin).

2.9 Purification of LUBAC by Size Exclusion Chromatography

Size Exclusion Chromatography (SEC) works by trapping smaller molecules in the pores of an adsorbent or stationary phase, effectively resulting in the delayed elution of smaller molecules compared to larger ones, thus allowing for the separation of proteins or protein complexes by their molecular weight. To further improve the purity of LUBAC samples, SEC experiments were conducted. For this, either Superdex 200 10/300GL (Cytiva) or Superdex S200 Increase 3.2/300 (Cytiva) was used depending on the protein quantities obtained from affinity chromatography. Columns were pre-equilibrated with 1 column volume (CV) of GF-Buffer (50mM HEPES, 150mM NaCl, 0.5mM TCEP, pH 8.0) before applying the sample.

2.10 Purification of LUBAC by Sucrose Gradients

Sucrose gradients are an effective technique for protein separation by mass. The underlying principle exploits the fact that denser particles will be pushed further in a viscous medium in the presence of a strong gravitational field than more dispersed particles. The

gravitational field can be generated by a centrifuge (100000 g). Stoke's law equation can be used to estimate the behaviour of proteins in solution,

$$v = \frac{d^2(p-L)g}{18\eta} \tag{2.1}$$

v: sedimentation rate

d: particle diameter

$p - L$: difference particle and medium density

g: gravitational acceleration

η: viscosity of the medium

This equation is not trivial to solve for sucrose gradients, as the medium density is not constant and changes over time. However, the sedimentation rate can be approximated by iterative methods [60]. Initially, a gradient tube is loaded with a low concentration sucrose solution (as low as 5%) on top of a high concentration sucrose solution (up to 40%). Centrifugation at high speeds will generate a radial distribution of sucrose concentration in the range of the solutions used, which is necessary so that bigger particles do not precipitate. The optimal centrifugation force and sucrose volume in the solutions is depend on the size (mass) of particles that should be separated. There is software available which can calculate the necessary centrifugation speed and time. In this thesis, 5-30% sucrose gradients were used for separating HOIL-SHARPIN dimers from LUBAC. After Strep-AC, 100 μL of a concentrated sample (1-2 mg/ml = 5-10 μM) were applied on top of the sucrose solution. The gradient was run at 60000 rpm (100000 g) for 16 h and 4°C (Beckman Coulter XE Ultracentrifuge, SW 60 Ti, 4 mL tubes). On the next day, the tubes were fractionated in volumes of 200 μL and analysed on stain-free gels.

2.11 Protein Concentration Measurement

Aromatic residues, like tyrosine and tryptophan, absorb UV light at 280nm. This property can be used to determine the molar extinction coefficient epsilon (L mol-1 cm-1) for the protein of interest and, therefore, the concentration of the sample using the Beer-Lambert law. The extinction coefficient was estimated based on the protein sequence using Expasy's ProtParam tool [61]. Protein concentration was then measured with a Spectrophotometer (DS-11 FX by DeNovix) using

$$c = \frac{A}{\epsilon d} \tag{2.2}$$

where, A is the measured absorbance (or $log_{10}(\frac{I_0}{I_{trans}})$), d the sample thickness, and c is the sample concentration.

2.12 Mass Photometry measurement of LUBAC

Mass photometry (MP) is a technique where binding events can be quantified individually by illuminating the interface between the sample and the cover glass. Reflectivity changes occur due to the change in the local refractive index when adhering biomolecules replace water. Individual proteins will adhere to the coverslip surface over time and the changes in reflectivity can be recorded interferometrically (see also 1, [62]). For MP experiments,

microscope coverslips (1.5, 24x50 mm, VMR) were cleaned with Isopropanol and Milli-Q by hand and subsequently dried with an N2 stream. A silicon gasket with 6 holes (3 mm diameter, Grace Bio-labs) was put on top of the coverslip to form chambers. LUBAC DCD samples were diluted to 0.2 mg/ml (equivalent to 1 μM). An 18 μl droplet of GF-Buffer (50 mM HEPES, 150 mM NaCl, 0.5 mM TCEP, pH 8.0) was placed in one of the gaskets holes, and the droplet was used to focus OneMP (Refeyn Ltd., Oxford, UK). Then, 2 μl of the sample were added and inverted by pipetting 3 times just before measuring. Movies of 1 minute at 100 fps were recorded and analysed using DiscoverMP software (Refeyn Ltd., Oxford, UK). By exploitation of the mass to contrast relation obtained from calibration with NativeMark ^{TM} Protein Std), which contains proteins species at 90, 180, 360 and 540 kDa, the analysed data could be converted to mass ($R^2 > 0.995$ for all calibrations).

2.13 Thermal Shift Assay, ProteoPlex

The denaturation and disassembly of LUBAC during plunge freezing might occur for numerous reasons, one being a wrong choice of the buffer. Thermofluor or Proteoplex ([63]) are techniques based on differential scanning fluorimetry (DSF), which allows determination of the optimal buffer conditions. In DSF, the protein of interest is added to a buffer screen containing different pH ranges and chemical components. Furthermore, a hydrophobic and fluorescent dye is added to the buffer screen. For each sample, the fluorescence upon gradually increasing temperature is measured. The resulting curve for most proteins consists of a fast exponential increase followed by a slower exponential decrease in fluorescence. It can be explained by a two-state unfolding process, meaning that the protein occupies only two states (e.g. folded and unfolded) while other intermediate states can be neglected. By applying thermal energy to the protein, it will start to unfold gradually, exposing the hydrophobic regions to the fluorescent dye, which, upon binding, will emit a signal. Once the proteins are completely unfolded, a peak in fluorescence can be observed [63]. However, further increases in temperature will reduce fluorescence as proteins will start to aggregate, reducing the binding area of fluorescent dye. For a two-state unfolding process, the fluorescence can be described by the Boltzmann equation:

$$F = F_{before} + F_{after} \frac{e^{C(T-T_m)}}{1 + e^{C(T-T_m)}} \tag{2.3}$$

F: Fluorescent signal

F_{before} and F_{after} : describe the temperature-dependent fluorescence signal before and after the transition

C: $\frac{\Delta H}{RT}$: a constant, which accounts for the influence of Enthalpy

T: Temperature

T_m: Melting temperature

The temperature at which the peak is reached depends on protein stability, which is influenced by the chemical environment provided by the buffer. Stabilizing buffers will therefore yield a higher fluorescence peak temperature, making Proteoplex a suitable method for determining the optimal buffer conditions. For this experiment, a master mix (420 μl LUBAC (prediluted to 2 mg/ml in GF-Buffer), 103 μl GF-Buffer (50 mM HEPES 8.0, 150 mM NaCl, 0.5 mM TCEP) and 2.1 μl SPYRO orange dye (prediluted in DMSO 1:5000) was prepared and 5 μl added to each fraction. The buffers used in the pH screen are displayed in the table 2.1.

Citric Acid (4)	Citric Acid (4.5)	Citric Acid (5)	MES (5.5)	MES (6)	MES (6.5)	HEPES (7.0)	HEPES (7.5)	HEPES (8.0)	HEPES (8.5)	Tris-HCl (9)	CHES (9.5)
Citric Acid (4)	Citric Acid (4.5)	Citric Acid (5)	MES (5.5)	MES (6)	MES (6.5)	HEPES (7.0)	HEPES (7.5)	HEPES (8.0)	HEPES (8.5)	Tris-HCl (9)	CHES (9.5)
Citric Acid (4)	Citric Acid (4.5)	Citric Acid (5)	MES (5.5)	MES (6)	MES (6.5)	HEPES (7.0)	HEPES (7.5)	HEPES (8.0)	HEPES (8.5)	Tris-HCl (9)	CHES (9.5)
Sodium phosphate (5)	Sodium phosphate (6)	Sodium phosphate (6.5)	Sodium phosphate (7)	Sodium phosphate (7.5)	Tris-HCl (7.5)	Tris-HCl (8)	Tris-HCl (8.5)	Gly (9)	Gly (9.5)	Gly (10)	Gly (10.5)
Sodium phosphate (5)	Sodium phosphate (6)	Sodium phosphate (6.5)	Sodium phosphate (7)	Sodium phosphate (7.5)	Tris-HCl (7.5)	Tris-HCl (8)	Tris-HCl (8.5)	Gly (9)	Gly (9.5)	Gly (10)	Gly (10.5)
Sodium phosphate (5)	Sodium phosphate (6)	Sodium phosphate (6.5)	Sodium phosphate (7)	Sodium phosphate (7.5)	Tris-HCl (7.5)	Tris-HCl (8)	Tris-HCl (8.5)	Gly (9)	Gly (9.5)	Gly (10)	Gly (10.5)
Bis-Tris (5.5)	Bis-Tris (5.5)	Bis-Tris (5.5)	Bis-Tris (6)	Bis-Tris (6)	Bis-Tris (6)	Bis-Tris (6.5)	Bis-Tris (6.5)	Bis-Tris (6.5)	Bis-Tris (7)	Bis-Tris (7)	Bis-Tris (7)
Bicine (8)	Bicine (8)	Bicine (8)	Bicine (8.5)	Bicine (8.5)	Bicine (8.5)	Bicine (9)	Bicine (9)	Bicine (9)	K/phos (7)	K/phos (7)	K/phos (7)

TABLE 2.2: ProteoPlex screen. MasterMix mixed into the buffer. The numeric value in brackets corresponds to the pH value.

2.14 Negative Staining

In negative staining electron microscopy, the contrast in a thin specimen is increased with an optically opaque substance (e.g. uranyl acetate). In this method, the proteins are embedded in a layer of stain. In an electron-microscope, the background will appear dark, because the opaque substance will absorb most of the electrons. In contrast, the protein will appear bright as its density is much lower [64]. It is important that the embedding layer is thin enough that the protein is not fully covered. If too much substance is used, the protein will also appear dark, and the image contrast disapears. Recombinant LUBAC was collected from fractions containing the peaks after SEC (Superdex S200 Increase 3.2/300 or Superdex 200 10/300). Cu grids (Agar Scientific G2440PF) were coated with a 3 nm thick continuous carbon support film and glow discharged for 1 minute at 200 mA and 10-1 mBar in a BAL-TEC SCD005 sputter coater (BAL-TEC, Liechtenstein). Samples were incubated for 1 minute at room temperature on grids before blotting away excess liquid. Grids were then stained with 2% (w/v) uranyl acetate, pH 4 (Merck) for 1 minute. Subsequently, grids were blotted again and left to air dry at room temperature for 20 minutes.

2.15 Grid Preparation

To perform single particle Cryo-EM, a thin layer of pure sample needs to be frozen rapidly on a grid that usually is made of a copper mesh or other metals, coated with holey carbon [47]. To conserve the structural integrity of the particles, the surrounding water in the solvent must not crystalize during freezing but vitrify. This is achieved by blotting using a filter paper to remove excess solvent, followed by plunging into liquid ethane [65], [66]. Furthermore, grids can be modified to optimize the signal-to-noise ratio and grid preparation in general. Graphene oxide support layer grids can be used in cryo-EM to make grids more hydrophilic and enhance the binding of biological macromolecules (removing them from the air-water interface) and allow for more uniform blotting during sample preparation [67]. In a recently developed method for graphene oxide grid preparation, grids are initially modified with PEI, a polycationic polymer, to increase the effectivity of GO sheets attachment to the grid. This method works under the assumption that grids have a slightly negative charge after plasma cleaning, as do the GO sheets. Coating the grid

with PEI changes the properties of the grid surface to a more positive charge, enhancing the binding of negatively charged GO. For this thesis, plunge freezing experiments with 2 different grid types have been conducted: a. Quantifoil 1.2/1.3 Cu200, b. graphene oxide grids with PEI [68].

1. *Copper grids*: For sample preparation, Quantifiol R 1.2/1.3 Cu200 Holey carbon grids were glow discharged for 90 s at 25 mA in a Bal-Tec SCD Sputter Coater, which was used to make the carbon more hydrophilic. Plunge freezing was conducted on a Leica EM GP. At a chamber humidity of 75% and 4°C, 4 μL of the sample was applied on the carbon side of the grid, immediately blotted for 2 s using a Whatman No.1 filter paper and plunged into liquid ethane.

2. *Graphene oxide with Polyethylimine (PEI, MW 40k)*: Quantifoil 1.2/1.3 Cu Mesh 200 washed with Chloroform and glow discharged for 60 s at 25 mA and 10-1 mbar. Graphene Oxide was diluted in a 1:8 ratio in Milli-Q and centrifuged at 1500 g for 1 minute to remove GO sediments. PEI was diluted to 0.1 mg/ml in 20 mM HEPES pH 7.9 just before use. 4 μL of PEI solution was applied on the glow-discharged carbon side of the grid and incubated for 2min, then washed 2 times with 4 μL of ddH2O (this step needs to be done quickly, to avoid dehydration as much as possible). Immediately, 4 μL of GO was applied on grids and incubated for 2 min before washing 2x with ddH2O again. Grids were plunge frozen on the same day as with time the grids become more hydrophobic.

2.16 Cryo-EM Tomography

Like CT scans in medicine, in electron cryotomography (cryo-ET) a series of 2D images at different angles can be combined to produce a 3D reconstruction. Usually, cryo-ET is used for imaging and studying macromolecules, viruses and even cells. In this study, Cryo-EM Tomography was used to determine the localization of proteins in respect to the AWI. LUBAC DCD (0.22 mg/ml = 1 μM) was applied on Cu 1.2/1.3, 200 grids and a tilt series on the in-house Glacios (Thermo Fisher) was conducted and processed. In total 61 images were taken with an increment of 1 degree. From the acquired images, a tomogram was generated in eTomo and movies, and snapshots for this thesis were made in 3Dmod [69].

2.17 Data Collection and Image Processing

Data was acquired on a Titan Krios G2 operating at 300 kV acceleration voltage, equipped with a Bio Quantum K3 detector (Thermo Fisher) and an energy filter. The acceleration voltage was 300 kV, spot size 6, C2 aperture 50μm and objective aperture 100μm. Images were collected at a magnification of 81 000x, corresponding to 1.07 Å/px, using the nano Pore EFTEM. The dose rate was 13.7 e/px/s or 12.19 e/A^2/s, with a total exposure time of 4 s this equals a total dose of 48.7 e/A^2 on the sample. A defocus range of -1.7 to -2.5 μm was used during collection. Importantly, Titan Krios G2 collects movies (not images). Each movie consists of a stack of single images. Recording movies instead of static images allows to conduct motion correction by comparing the frames. On one hand, the whole frame might drift due to movements of the stage; on the other hand, the electron beam will induce anisotropic motion of the particles. These beam-induced displacements would influence the precision of the reconstruction. However, motion-correction software can process micrographs on the fly and align frames, so the drift can be compensated. Once the micrographs were motion-corrected, 500 LUBAC particles were manually picked in CrYOLO [70] with a boxsize of 256 px (=270 Å) and used for CrYOLO model training. The

trained model was subsequently used for automated particle picking, resulting in a total of 190 000 particles picked. These were imported to cryoSparc2 [51] for further processing. From an initial (reference-free) 2D classification with 200 classes, of which 37 were selected, and 2D classification was repeated 3 times in total. This iterative approach allowed to remove particles with low purity (low cross-correlation with 2D template). The final iteration resulted in a total of 130 000 particles selected, which were used for Ab Initio reconstruction. Ab Initio reconstruction did not generate a model with sufficient quality, as it did not appear to include the whole LUBAC complex. Processing was therefore not continued after this step. 3D classification and postprocessing would likely generate artefacts.

2.18 CrYOLO

CrYOLO is a machine learning software for automated particle picking in cryo-EM. CrYOLO requires training a convolutional neural network (CNN). Practically, this is achieved by manually picking roughly 400–1000 particles from several micrographs (20-50 micrographs, depending on protein concentration). After training, each micrograph is split into a grid of single cells. For each cell, crYOLO calculates the confidence that a particle is within that given cell. If a particle was found (the user can change the threshhold), the relative position of the particle centre to the cell centre is estimated by applying regression [71]. In this thesis the trained CrYOLO model picked 190 thousand particles automatically, which were further processed in cryoSparc2.

2.19 AlphaFold2

Alphafold2 is a deep learning program that uses a novel approach to predict the three-dimensional structure of proteins solely on their amino acid sequence. The structure prediction is calculated by incorporating neural network architectures based on physical, geometrical, and evolutionary constraints of protein structures. The Alphafold2 network comprises of two main stages. First is the trunk, which processes the inputs through repeated layers of the neural network: here the network extracts information on 3D structure from multiple sequence alignment. The second main stage is the structure module, which introduces a 3D by rotation and translation of every single protein residue. Compared to other computational approaches, AlphaFold2 is able to predict protein structures with higher certainty [72]. In this thesis, AlphaFold2 was used to estimate LUBAC's 3D structure and volume diameter. Because the proteins seemed to disassemble on the grid, the structure prediction was used to generate a 3D template that was used for 3D reference-based automated particle picking from the micrographs. This approach ensures that picked particles are of an anticipated size. A 3D map for the whole LUBAC sequence (consisting of single subunits or of combinations of domains) was generated in ChimeraX molMap function [73] using the AlphaFold2-predicted structure. 3D Templates were generated in cryoSPARC2 ('Create Templates'). The processing pipeline resembles the steps described in data collection. Ab Initio map was then compared to several structure predictions of a combination of subdomains of HOIL, HOIP and SHARPIN.

Chapter 3

Results

3.1 Overview and Objective

Obtaining the structure of LUBAC is necessary for understanding the formation of linear linked Ub-chains and thus the activation of the NFκB pathway. Cryo-EM is a suitable method to obtain high-resolution structures of proteins in a near-native state. The general pipeline in cryo-EM starts with purification of the protein of interest, usually followed by biophysical characterization to ensure sufficient sample quality. In rare cases, the structure of the protein of interest can be reconstituted directly after purification. However, for most proteins, it is necessary to optimize purification and grid preparation steps. Numerous reasons may cause a drop in resolution or failure of Reconstruction, such as inappropriate selection of buffers, highly flexible domains, dissociation of the protein or adsorption to the air-water interface (AWI), to name a few. As it turned out, LUBAC is a challenging protein in that regard. Therefore, different purification and grid preparation techniques were applied and optimised to increase the resolution in reconstructed LUBAC volumes. A flowchart of the cryo-EM pipeline applied in this thesis is shown in Fig. 3.1. Different chromatography techniques were used to elute LUBAC only, without any contaminants. ProteoPlex experiments were conducted to find ideal buffer conditions for LUBAC. Optionally, LUBAC was modified by binding it to one of its substrates or E2 partners to stabilize LUBAC. Similarly, crosslinking was used to decrease the dissociation of LUBAC during cryo-EM grid preparation. Various grid preparation methods were applied to facilitate the immersion of particles into the ice and prevent particles from adsorption to the AWI. Once purification and grid preparation were optimised, LUBAC data was acquired, processed, and analysed. This thesis obtained a low-resolution structure for the E3 ligase LUBAC, which will be presented at the end of this chapter.

3.2 LUBAC Purification from SF9 cells

The E3 ligase LUBAC consists of three subunits, namely HOIP, HOIL and SHARPIN, which have molecular weights of 120, 60 and 43 kDa, respectively. The LUBAC construct used in this thesis expressed all three subunits with an N-terminal Strep-tag on SHARPIN and an N-terminal His6-Tag on HOIL. Furthermore, two modified constructs were generated: LUBAC HOIL-GFP, which has a C-terminal GFP tag attached to HOIL-1L and LUBAC DCD, a double mutant variant with mutations on HOIL-1L (C460A) and HOIP (C885A). These mutations inhibit the catalytic function of HOIL-1L and HOIP (Fig. 3.2). Sf9 cells were infected with the corresponding baculovirus for each construct and subsequently purified by running the cell lysate on Strep-AC followed by Size Exclusion Chromatography (SEC). The fractions were visualised with SDS-PAGE using stain-free gels, which revealed a 1:1:1 stoichiometry of HOIP, HOIL-1L and SHARPIN (Fig. 3.2 a, Supp. Fig. 5.3). However, similar results were obtained for LUBAC WT and LUBAC HOIL-GFP

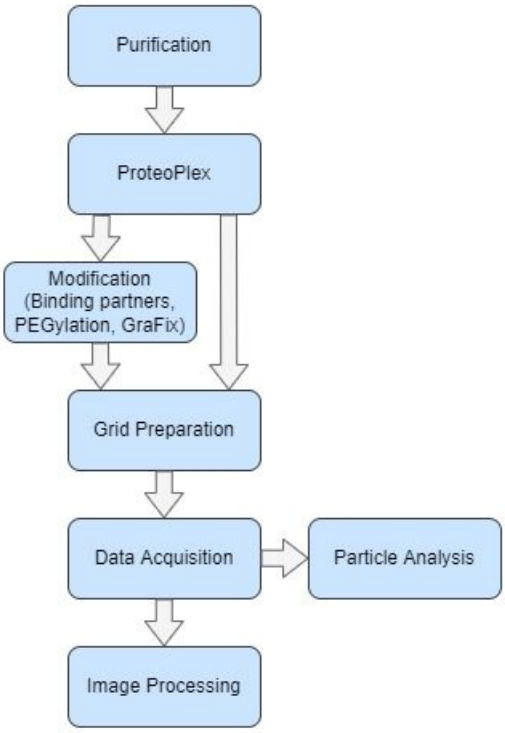

FIGURE 3.1: Experimental pipeline used in this thesis

constructs (Supp. Fig. 5.1) with elevated HOIL bands for LUBAC-HOIL-GFP. The purification of LUBAC DCD seemed to have the highest yields and best stoichiometry compared to the other two constructs. As LUBAC DCD and LUBAC WT have identical structures, LUBAC DCD was used for cryo-EM sample preparation. Fractions 15 and 16 showed the highest protein concentrations with desirable stoichiometric properties (Fig. 3.2 a). These fractions, however, co-elute with an additional band at 250 kDa. Initially, this band was considered LUBAC aggregates as samples were not boiled before SDS-PAGE. However, boiling the sample before application on gels did not remove the additional band. The fractions were therefore submitted to our in-house mass-spectrometry facility (Supp. Fig. 5.2). The additional band was identified as Acetyl-CoA-Carboxylase 1 and 2 (ACC1, ACC2). With a molecular weight of 250kDa (ACC1) and 270kDa (ACC2), they were similar to the molecular mass of LUBAC (222kDa). ACC cannot be separated in Strep-AC because it has a biotinyol domain, which has a strong affinity for the immobilised Strep-Tactin on the column. As a result, strep-AC led to the copurification of ACC with LUBAC. Due to their similar size, they could not be separated by SEC. This problem was resolved by on-column cleavage of the Strep-Tag of SHARPIN. Whilst the ACC remained bound to the strep column, cleaving the Strep-tag off LUBAC resulted in its release from the column, free of contaminants. The ACC remained immobilized on the column resin. LUBAC was not bound to the resin so that it could be washed off with GF-Buffer (W fractions in Fig. 3.2 b). The ACC was eluted by applying desthiobiotin buffer to the column (E fractions Fig. 3.2 b).

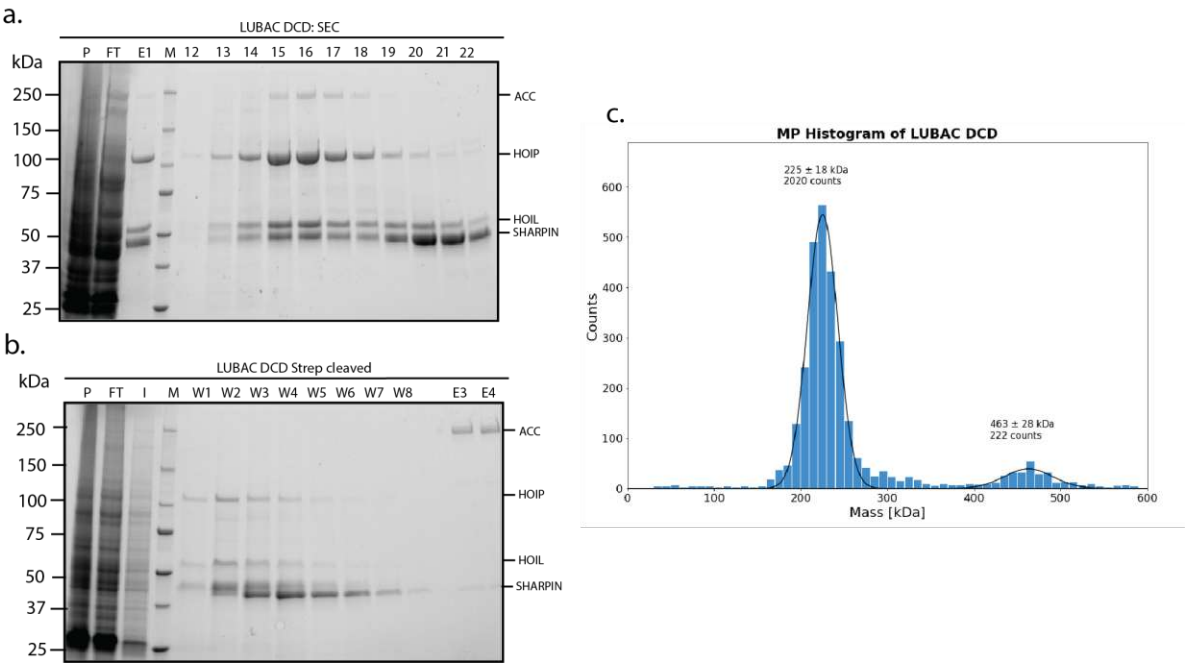

FIGURE 3.2: Purification of LUBAC DCD. (a) LUBAC DCD purified by Strep-AC and SEC. The contaminant ACC is visible in LUBAC fractions. (b) On column Strep cleavage. Fractions W depict the washing step, while E-fractions show elution steps with desthiobiotin. (c) Mass Photometry Histogram of LUBAC DCD (222 kDa). Low amounts (10%) of LUBAC dimers (444 kDa) remain in the sample. P = Pellet, FT = Strep-Flow-Through, E1 = Input sample for SEC and I = Fraction eluted during injection of 3C-Precission Protease.

3.3 Thermal Shift Assay

A buffer screen (Fig.3.3) was set up to increase sample quality before optimising purification and grid preparation steps to determine ideal buffer conditions for LUBAC. A poor or unfortunate choice of a buffer may facilitate LUBAC dissociation during cryo-EM grid preparation. Measuring the unfolding of LUBAC in the ProteoPlex experiment, a thermal shift assay, allows for analysing buffers by their highest melting temperature and thus stability. In general, LUBAC was found to be most stable in buffers with pH above the physiological pH. Furthermore, out of the ten buffers with the highest score, only one had a pH below 8.5. Bicine pH 8.5 achieved the highest melting temperature score (Fig.3.3 a). Following this experiment, purification of LUBAC DCD was carried out in buffers containing Bicine pH 8.5 to determine the influence of buffer type and pH on LUBAC behaviour. No significant improvement was observed compared to the previously used HEPES pH 8.0 buffer. MP measurements showed similar species distributions for both buffer and pH types (Fig.3.3 c), and LUBAC particles still appeared to dissociate during cryo-EM grid preparation (Fig.3.3 d). The two buffers had melting temperatures of 57°C and 56°C, respectively, explaining the similar results obtained from MP and cryo-EM. In conclusion, this ProteoPlex experiment confirmed that the initial buffer (HEPES pH 8.0) used for purifications provided good characteristics for LUBAC and advised against buffers with lower pH. Therefore, the low sample quality was not due to buffer conditions, and thus other ways to improve the sample were sought after.

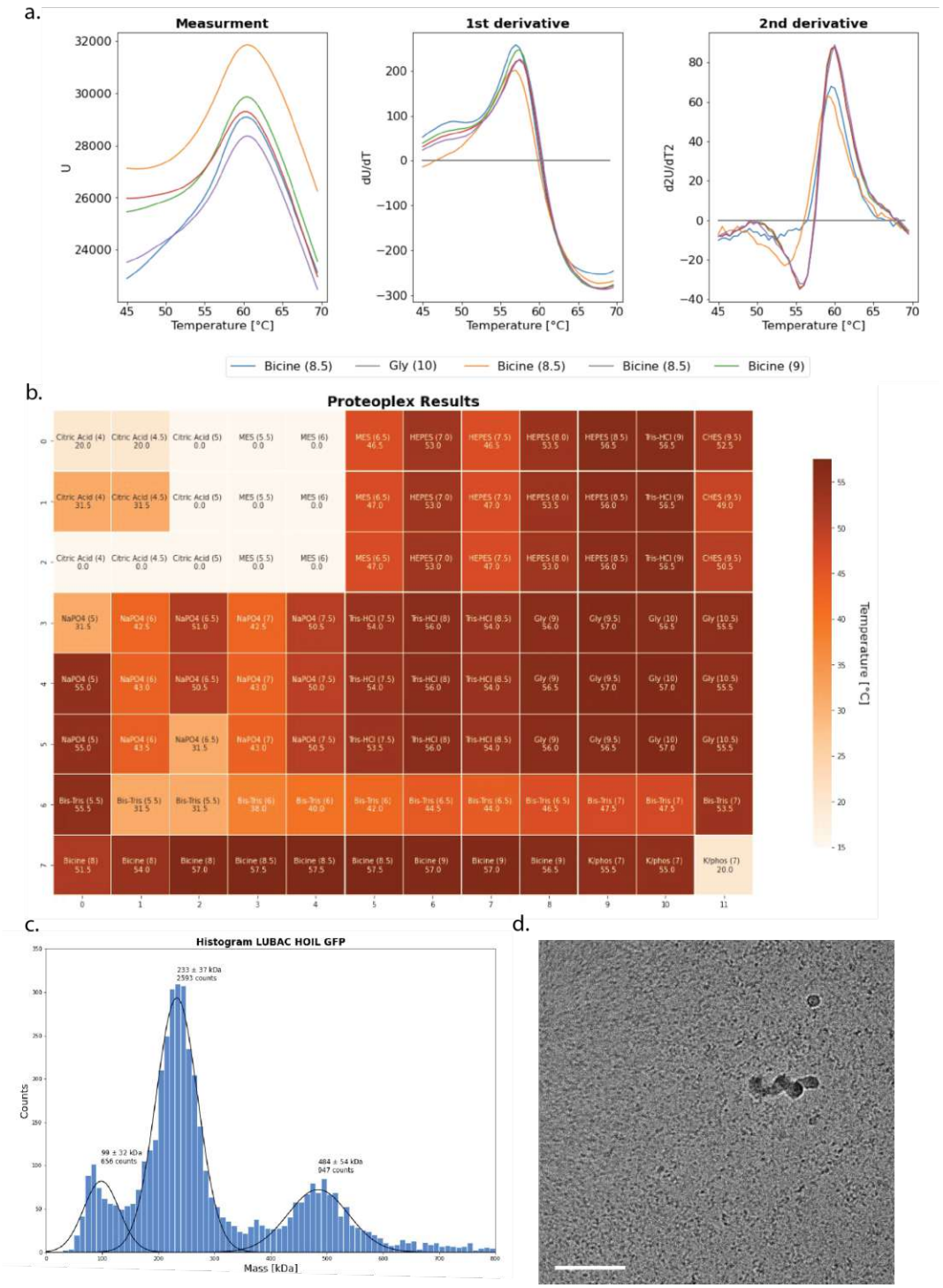

FIGURE 3.3: ProteoPlex of LUBAC. (a) melting curves and their 1st and 2nd derivatives of the top 5 buffers. The zero point of the 2nd derivative equals the melting temperature as it resembles the turning point in the fluorescence measurement. (b) Heatmap of the buffer screen. pH Buffer increases from left to right. Buffers with Tm = 0 result from non-fitable data. Temperature scale starts at 15°C (white) and ends at 55°C (brown) (c) MP measurement of LUBAC HOIL-GFP after SEC with Bicine pH 9.0. (d) cryo-EM image of a sample from (c). Bars equal to 100 nm

3.4 LUBAC purification using Gradients and GraFix

Besides the SEC purification, gradients were also used to separate LUBAC from other proteins, single subunits or LUBAC dimers. Using gradients in sample preparation provides gentler means of separating protein complex subspecies. This might lead to more homogeneous protein complexes that are better suited for cryo-EM than chromatography purified samples. Similarly to the SEC purification, the separation of the LUBAC and HOIL-SHARPIN dimers could be achieved (Fig. 3.4 b, 3.4 d). Furthermore, the gradient method was expanded to Gradient Fixation (GraFix) by using different crosslinkers that help stabilize and fixate protein complexes. A titration series with BS3 and GA crosslinked LUBAC DCD samples were conducted to estimate the ideal crosslinker concentration (Fig. 3.4). For BS3 and GA, this resulted in ideal crosslinking concentrations of 250 μM (50x molar excess) and 0.01 – 0.02% in GF-Buffer, respectively. Using a too high concentration can result in the aggregation of LUBAC complexes. Subsequently, gradients with similar ratios of sample to crosslinker have been set up and run with controls (Fig. 3.4 b, d). Crosslinked samples showed smeared bands and some additional bands at higher molecular weights, showing that crosslinking was successful. To further investigate the quality of the samples and to validate that the crosslinking did not contribute to the aggregation of the sample, MP experiments have been conducted (Fig 3.4 e). Samples treated with 0.01% GA showed an overall higher percentage of LUBAC dimers by about 5%, which is in the range of measurement deviation. It can be concluded that LUBAC remained in a relatively native state with almost no aggregation. The crosslinked protein was anticipated to be more stable and, therefore, not dissociate in solution. However, observation of cryo-EM images showed that the particles did not resemble the full LUBAC. This led to the hypothesis, that plunge freezing might induce a hostile environment for particles.

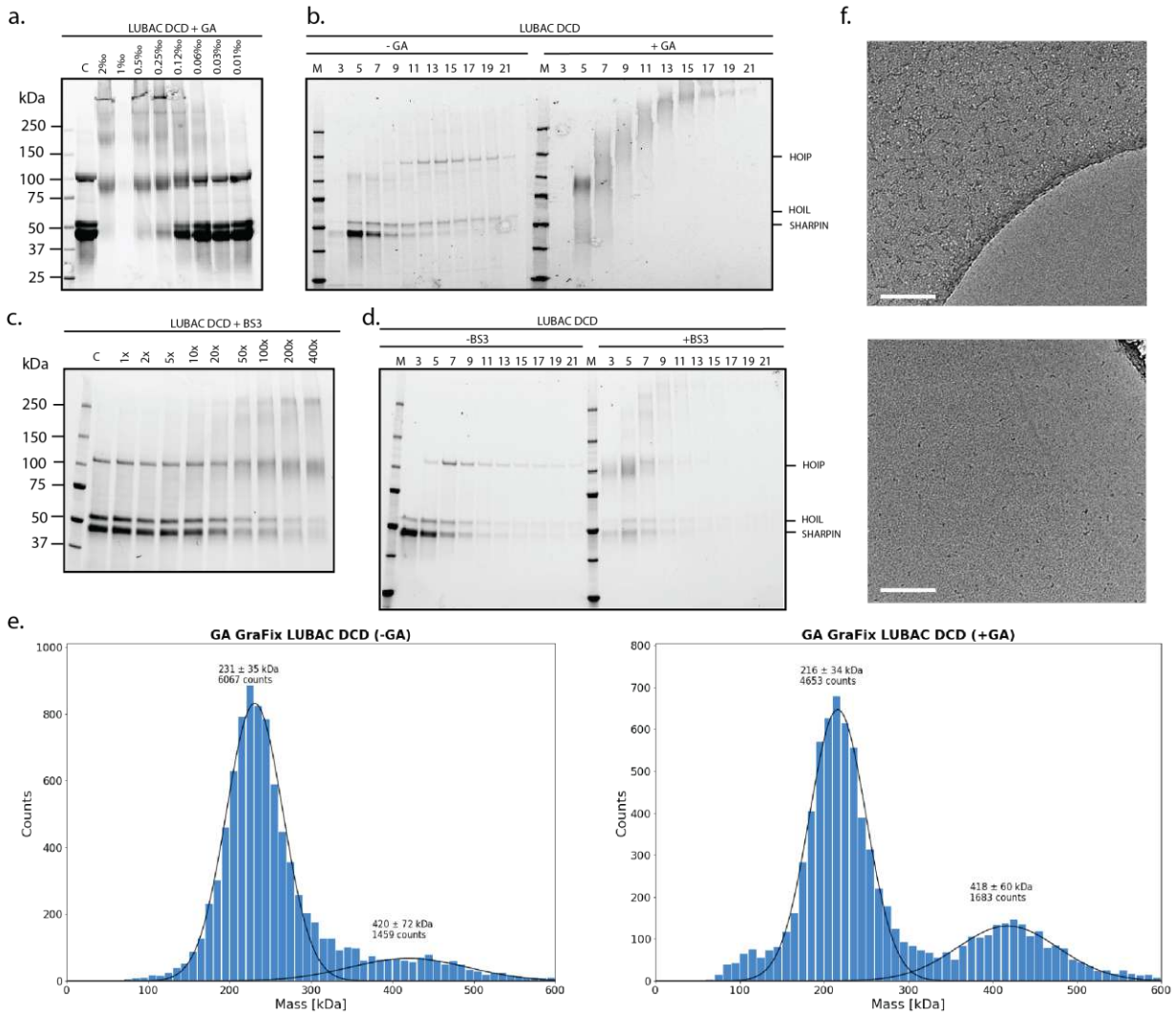

FIGURE 3.4: Purification of LUBAC by Gradient and GraFix. (a) Titration series with GA revealed 0.0015% as a good concentration for GraFix experiments. (b) GraFix with LUBAC DCD and GA (0.0015%). (c) Titration series with BS3 revealed 50x molar excess as a good concentration for GraFix experiments. (d) GraFix with LUBAC DCD and BS3. (e) MP measurements of crosslinked LUBAC DCD (right) and control (left) (f) examples of particle distribution of BS3 crosslinked samples on 1.2/1.3 Cu 200 grids. It appears that the majority of particles remain on carbon lattice. Bars equal to 100 nm

3.5 LUBAC substrate binding

Stabilizing a complex by binding it to one of its substrates or other proteins might improve particle quality in cryo-EM. This is because the attachment of additional proteins might give more structure to unstructured regions, thus increasing stability and homogeneity. Generally, larger particles are easier to pick and align during automated particle picking and image processing. Therefore, to improve cryo-grid preparation, two potential binding partners of LUBAC were used: OTULIN, a deubiquitinase which binds to HOIP with high affinity, and NEMO, a substrate of LUBAC ([10], [74]). To validate the binding of LUBAC to these proteins, sucrose gradient sedimentation was performed. Should two proteins interact, their sedimentation profile in the gradients would be changed, as higher kDa complexes sediment in higher sucrose. However, our experiments could not confirm the binding of LUBAC to OTULIN. Compared to the controls, an anticipated shift of OTULIN-bands and NEMO-GFP bands to higher fractions did not occur (Fig. 3.5). NEMO and OTULIN bind LUBAC only transiently, and the formation of stable complexes does not occur. While NEMO has not been reported to bind LUBAC directly, OTULIN was shown to have a strong affinity for the PUB-domain of HOIP. This behaviour was not observed in the gradient sedimentation experiments with LUBAC WT, suggesting that the affinity is HOIP-specific.

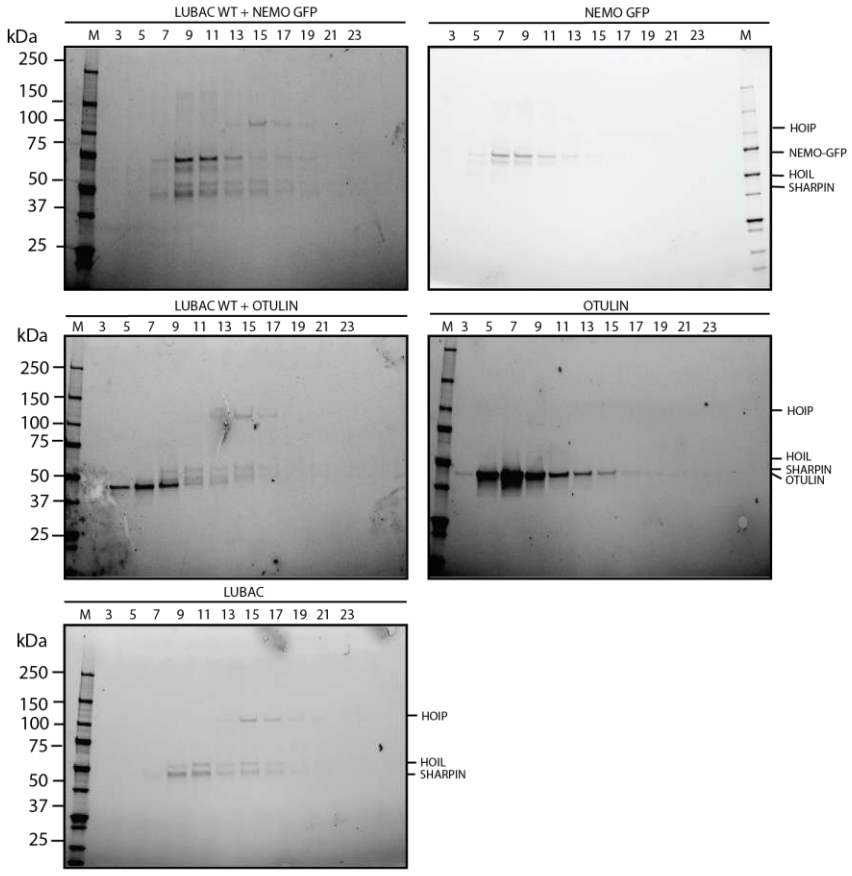

FIGURE 3.5: Stain-free gels of each second fraction from gradient experiments. LUBAC WT was incubated with OTULIN for 1 h on ice before applying the sample to the gradient. The same was performed for NEMO. NEMO and OTULIN-only gradients were used to determine if a shift occurred due to complex formation.

3.6 LUBAC and E2-parnter interaction

Two other potential interactors were examined in a further attempt to increase the stability of LUBAC. These are two E2 ligases, Ubch5b and UbcH7, which, together with LUBAC, initiate the formation of elongation-free ubiquitin chains in vitro. Sucrose gradient sedimentation was performed as with the previous potential interaction partners to study their interaction. While UbCH7 showed a minimal shift in the gradients, the bands of UbCH5b were shifted by approximately 3 fractions in gradients containing LUBAC WT, suggesting an interaction. To further validate this interaction, an MP measurement was performed. Indeed, analysis of fraction 7 of the gradient showed that UbcH5 binds HOIP alone (137 kDa), while large amounts of HOIL-SHARPIN subcomplex (100 kDa) remain. Similarly, fraction 13 was analysed with MP to inspect potential UbcH5b-LUBAC formation. Surprisingly, only very low quantities of full LUBAC complex could be detected. This might be due to the overall low concentration of HOIP compared to SHARPIN (Fig. 3.6 a-b), which is necessary for LUBAC formation. Nevertheless, the affinity of UbcH5b towards HOIP could be detected. These results showed that Ubch5b binds HOIP but not the HOIL-SHARPIN subcomplex. The observation raises the question of whether the LUBAC trimer only forms transiently and exists predominantly as HOIP and HOIL-SHARPIN. This would be a possible explanation for the preference of Ubch5b for the HOIP subunit only and why non-crosslinked LUBAC dissociates on cryo-grids.

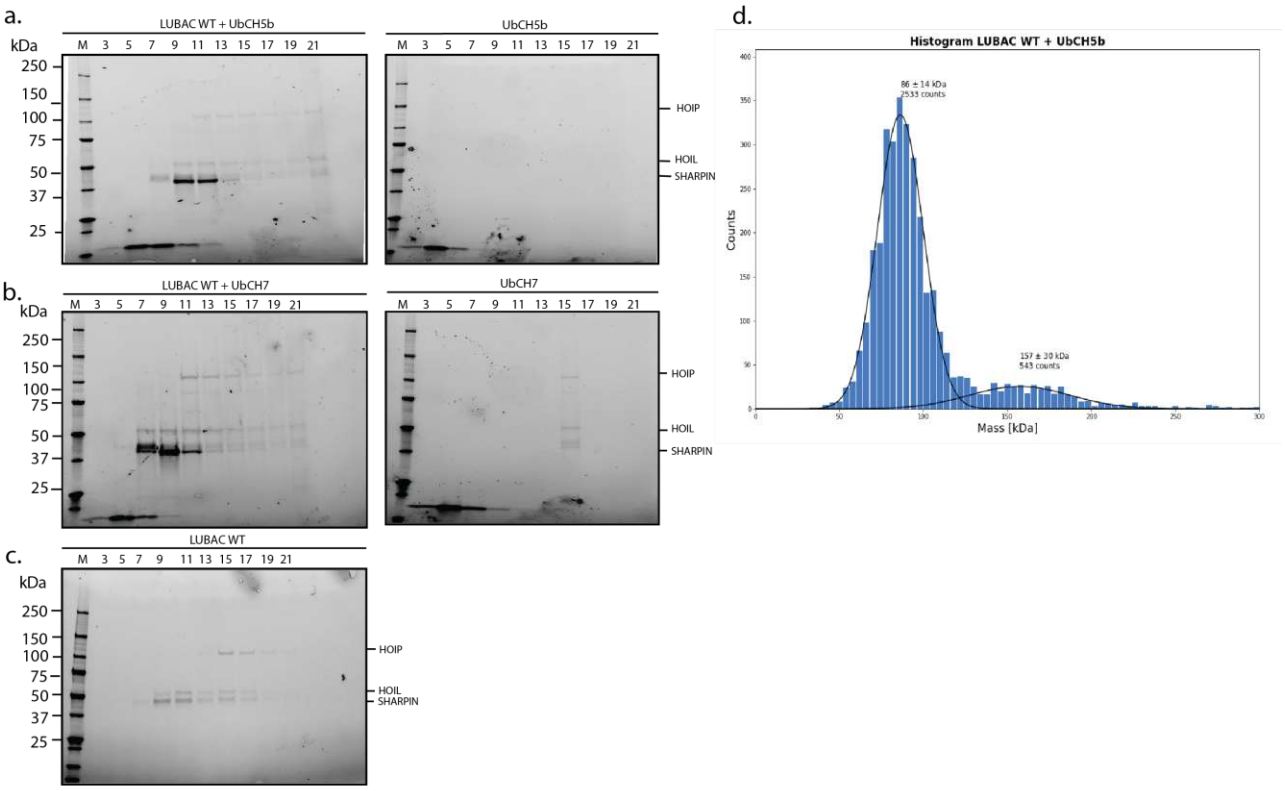

FIGURE 3.6: Gradient of LUBAC WT and E2 Ligases. (a) LUBAC WT was incubated with UbCH5b for 1 hour on ice before application on the gradient. The gel on the right shows the control with UbCH5b alone. (b) LUBAC WT was incubated with UbCH7 for 1 hour on ice before application on the gradient. The gel on the right shows the control with UbCH7 alone. (c) LUBAC WT Control Gradient (d) MP results for fraction 9 of LUBAC WT + UbCH5b gradient.

3.7 Autoubiquitination of LUBAC

In this thesis, all three constructs were performed ubiquitination assays to determine if the enzymes are biochemically active and thus functional. LUBAC DCD has two point mutations at C460A and C885A, which should inhibit the autoubiquitination of LUBAC. Time-series experiments for each construct incubated with free fluorescent Ubiquitin were carried out and analysed by fluorescent illumination. Images of the stain-free gels were acquired as a control for the presence of LUBAC components (Supp. Fig. 5.4), as only the subunit HOIL-GFP is visible by fluorescent illumination. Indeed, auto-ubiquitination was observed for LUBAC WT and LUBAC-HOIL-GFP construct, but not for LUBAC DCD (Fig. 3.7, Supp. Fig. 5.4), validating the catalytical inactivity of the LUBAC DCD construct.

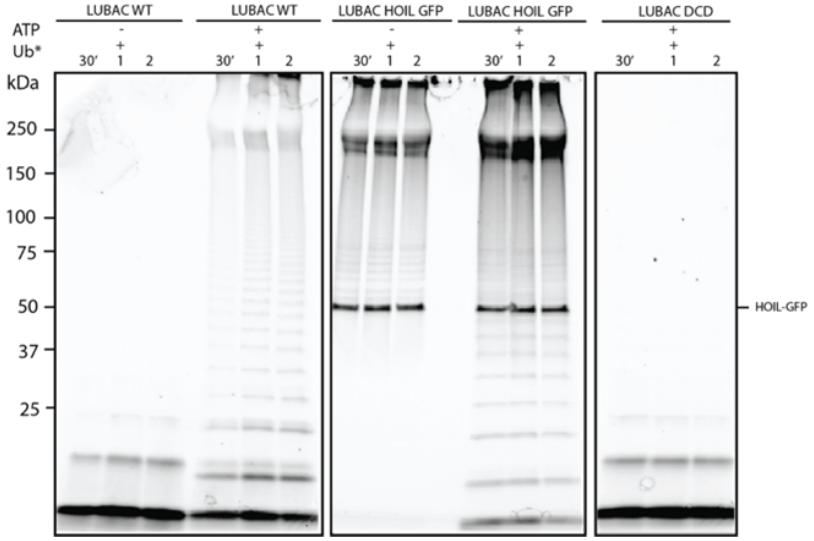

FIGURE 3.7: Ubiquitination assay with LUBAC WT, LUBAC HOIL-GFP and LUBAC DCD. Mutations on LUBAC DCD (C460A and C885A) inhibit the catalytic activity of LUBAC. Gels were imaged with the fluorescein channel to visualize fluorescent ubiquitin.

3.8 Effects of Centrifugation on Particle Integrity

In most cases, LUBAC samples needed to be concentrated after SEC to a concentration of at least 1 μM for freezing. However, concentrating might influence protein assembly as shear forces could disassemble the complex during this process. Because of the problematic behaviour of LUBAC on cryo-grids, samples before and after concentration were analysed with mass photometry to investigate the effects of concentrating on LUBAC. The experiment verified that centrifugation had no impact on protein disassembly (Fig. 3.8). As concentration is the last step before plunge freezing, it can be concluded that the main problems regarding the imaging of LUBAC are not due to concentrating.

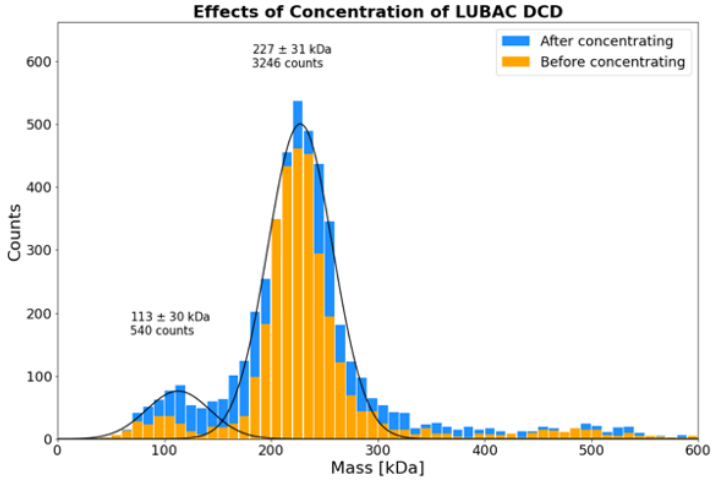

FIGURE 3.8: [Effects of Centrifugation on species distribution. The orange graph represents the sample before concentrating and the blue after concentrating. Data is not normalised.

3.9 Grid Preparation with Detergents and Graphene Oxide

This thesis showed that the optimization of LUBAC samples concerning their integrity and homogeneity was achieved by implementing various methods. The purpose of these techniques was to stabilize LUBAC particles, increase contrast during image acquisition and provide sufficient purity for classification. Similarly, grid preparation needs to be optimised as grids introduce environmental changes for the particles. There are numerous possibilities of how grid preparation can be altered. Grid materials, coating, geometry, and plunge freezing parameters all affect the immersion of particles in ice. Furthermore, the use of detergents can positively change particle distribution. These parameters should be considered to ensure the optimal grid environment for particles. During initial data acquisition, LUBAC seemed to prefer the AWI and dissociate during vitrification. Therefore, a variety of different freezing approaches were introduced to improve particle quality: one of them being the use of detergents. Detergents block particles from adhering to the air-water interface by occupying it, thus blocking particles from reaching it. Grids with LUBAC were supplemented with several detergents just before freezing and subsequently screened. The list of detergents included 0.02% CTAB, 0.05% beta-glucoside, 0.0005% LMNG and 4 mM CHAPSO. Because detergents seemed to push particles out of the grid holes, the initial LUBAC concentration was increased. However, grids modified with detergents seemed to neither improve particle stability nor prevent LUBAC from migrating to the AWI. A collection of micrographs from detergent screening is provided in the supplementary section (Supp. Fig. 5.5). Furthermore, grids with graphene oxide (GO) support layers were used, which are naturally more hydrophilic and help particles spread more evenly. The change in environment could aid in relocating the protein from the AWI into ice. The thickness and the homogeneity of GO were tested by analysing empty grids in the diffraction mode (Fig. 3.9 a). Due to graphene's hexagonal lattice, its diffraction pattern consists of 6 hexagonal assembled dots for single-layer graphene. If two or more layers are present, an additional hexagonal ring shifted by 30 degrees is visible. It is not possible to distinguish between 2 or more layers because the third layer would have a shift of 60 degrees, which overlaps with the first layer. However, if the graphene lattice is

broken, additional diffraction points may be visible. As only two dots were observed in the diffraction pattern, it is likely that the graphene lattice presented here has little to no fractures (Fig. 3.9 a) and consists of at least 2 layers. While the commercially bought GO grids did not improve sample quality, self-made PEI-GO grids using the PEI preparation method ([68]) seemed to improve overall ice quality. Grid squares were fully covered in a thin film of ice with homogeneous distribution over whole grid squares. Nevertheless, LUBAC was concentrated in dry regions or regions with very thin ice (Fig. 3.9 c), implying its preference for the AWI.

3.10 Tomographic Analysis of the Air-Water-Interface

Several approaches to freezing LUBAC were attempted, including detergents and different grid types. In all cases, LUBAC seemed to concentrate in dry regions and dissociate. Most likely, LUBAC particles adhere to the AWI, where they lose their structure due to exposure to air. To validate this hypothesis, a tilt series was collected for tomogram reconstruction. Figure 3.9 d shows a side view of one of the grid holes. The ripple at both ends of the recording represents the carbon support film. Particles appear as small dots (circled in orange). In this LUBAC sample, the particles concentrated at the upper meniscus; at the air-water interface. From this experiment and due to the failure of previous classification attempts, it can be concluded that the disassembly of LUBAC is, at least partially, caused by the exposure to the interface. These issues need to be addressed by either changing the plunge freezing procedure (e.g. Chameleon) or optimizing the solution buffer (e.g. with detergents). The advantage of using time-resolved cryo-EM techniques (Chameleon) is that the time frame between applying the solution on grids and freezing the grid is extremely short. Particles have very little time to diffuse to the AWI and are more likely to be immersed in ice/solution.

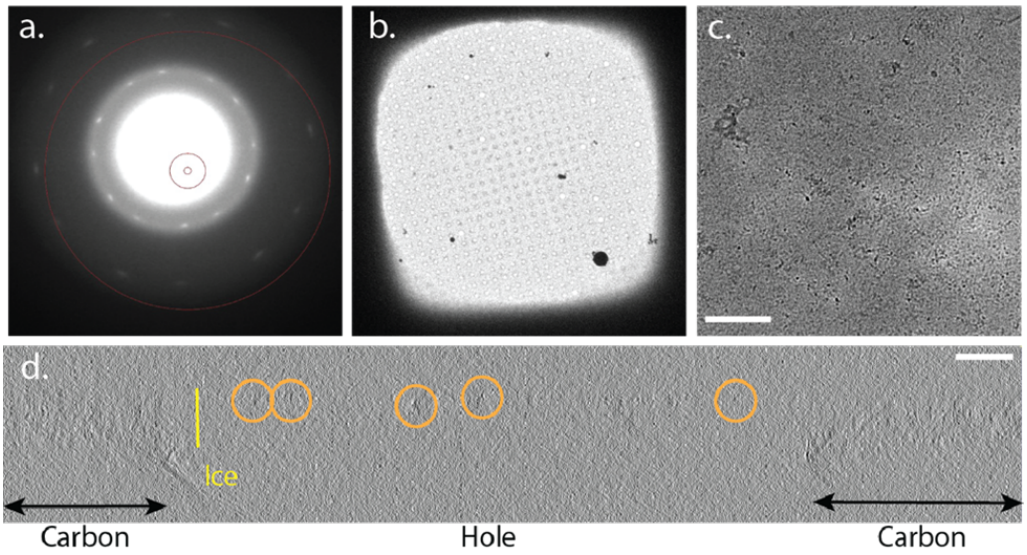

FIGURE 3.9: Cryo-Electron tomography and the air-water interface.(a) Diffraction pattern of empty GO-grid. Hexagonal rings of two layers shifted by 30 degrees are visible. Likely there are more than two layers present. (b) Grid square of GO-grid: ice covers almost all holes with homogeneous distribution. (c) cryo-EM image of LUBAC DCD on GO-grids. (d) Tomogram of LUBAC DCD: Sideview obtained from Tilt Series of LUBAC DCD 1 μM on 1.2/1.3 Cu 200 grids. Carbon support film is visible on both sides. Particles are circled in orange.

3.11 PEGylation and negative Stain

As detergents did not seem to prevent the adsorption of LUBAC to the air-water interface, other methods were considered. A recent paper proposed a new method of chemically modifying the protein of interest with PEG [75]. This reagent specifically PEGylates lysine and N-terminal primary amines and covers the protein in a PEG mask that protects it from aggregation and exposure to the air-water interface during vitrification. In this work, LUBAC-HOIL-GFP was modified with PEG12 before running SEC and a gradient subsequently (Fig. 3.10 a-b). The bands of LUBAC modified with PEG12 were smeared, indicating that PEGylation was successful. Similarly, analysis of MP displayed broader peaks, most likely due to different amounts of attached PEG12 on single LUBAC particles (Supp. Fig. 5.6). The samples were then further analysed by negative staining. However, compared to the untreated sample, PEGylation of LUBAC did not seem to improve overall particle stability, as judged by comparing negative stain images. On the one hand, less aggregation was visible, but on the other hand, particles seemed to dissociate more than in the control sample.

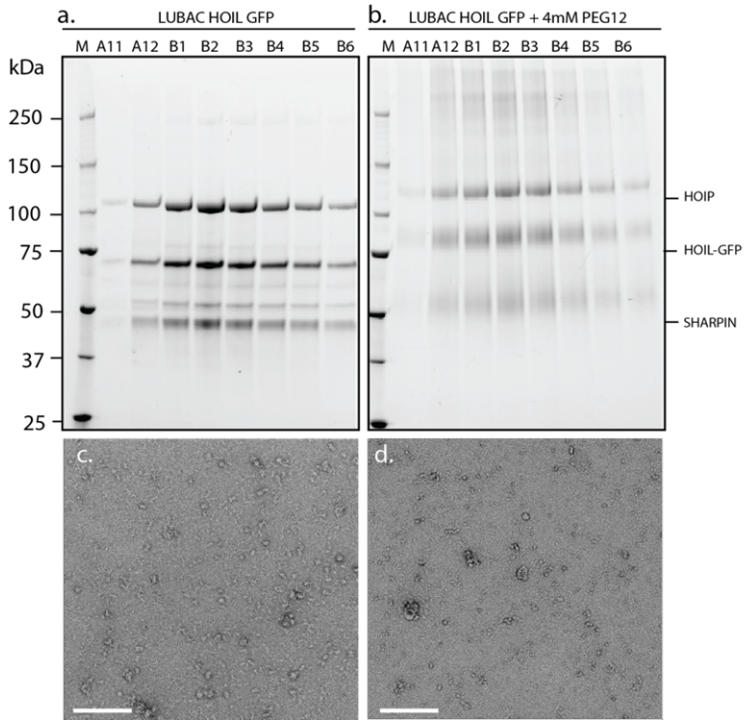

FIGURE 3.10: PEGylation of LUBAC HOIL-GFP. (a) Control gradient LUBAC HOIL-GFP (b) LUBAC HOIL-GFP gradient incubated for 30 min with Methyl-PEG12-NHS before running it on SEC and a gradient. (c) negative stain of LUBAC HOIL-GFP (d) negative stain of LUBAC HOIL-GFP modified with PEG12.

3.12 Structural Reconstruction of LUBAC

3.12.1 Image Processing and Ab Initio Reconstruction

After validating the purity, integrity, and homogeneity and finding suitable grid preparation conditions, image data for single particle analysis (SPA) was collected. However, data acquisition of the LUBAC sample with good particle distribution and contrast was challenging, mainly due to the absorption of particles into the AWI (see previous chapters). Nevertheless, a low-resolution structure of the complete LUBAC complex could be obtained. Particles still could be classified in cryoSparc (Supp. Fig. 5.7 a), and a low-resolution map of LUBAC could be reconstructed (Fig. 3.11 a). The general pipeline used for image processing in this thesis can be found in the methods and materials section. The obtained structure had a resolution of 9.4 Å. Although this is too low to gain structural insight into the generation of linear Ub-chains, a rough shape of LUBAC can be estimated from this map. It appears that this map represents not the whole LUBAC protein. The anticipated minimal radius for a spherical protein of 220 kDa is about 80 Å. Although the obtained map nicely fits this value, it is important to consider that LUBAC is not spherically shaped. Therefore, the maximum diameter of the map is expected to exceed 120 Å. As a variety of crystal structures of different domains of LUBACs already exist, I attempted to fit some of them into the map. Interestingly, the trimeric core of LUBAC (PDB: 5y3t), which consists of the UBL, UBA and UBL domains of HOIL, HOIP and SHARPIN, respectively, could be fitted into the map (Fig. 3.11 b). These observations led to the hypothesis that LUBAC might be very flexible in peripheral regions, while the trimeric core is relatively static and stable. The movement of these regions causes a drop in signal-to-noise ratio and effectively in resolution. A small volume right next to the core was present in all Ab Initio models. Most likely, this volume represents one part of the peripheral parts of HOIP, HOIL or SHARPIN. As shown in the previous section LUBAC tends to be exposed to the AWI, which may cause dissociation of the protein. The adsorption to the AWI and the flexible properties of LUBAC is most likely the cause of the absence of the peripheral regions on the map.

3.12.2 “In Silico” Reconstruction

The findings in the previous section led to the question of what are the structural arrangements in the LUBAC complex and what effects impede the resolution of the peripheral regions. Under the assumption that LUBAC is relatively flexible and that some of the picked particles were dissociated, particle picking in crYOLO might pass on a high percentage of “broken” particles to Reconstruction. This would result in a poorly trained picking model and hence incorrectly classified particles. With the introduction of AlphaFold2, a heuristic approach could be attempted that does not require machine learning at all. The LUBAC sequence was used to predict the structure of the LUBAC complex by AlphaFold2 (Fig. 3.12 a). Subsequently, using the molMap command in ChimeraX, a map with a virtual resolution of 8 Åwas generated. Instead of training a model with crYOLO, this map was used as a template for automated picking in cryoSparc. The advantage of this approach is that particle picking selects particles with the anticipated dimensions. Afterwards, the same processing pipeline as for the Ab-Initio1 was used. This approach’s LUBAC structure (Ab Initio 2) was very similar to Ab-Initio1 (Fig. 3.11 c). The Ab Initio maps presented here are both of roughly 80 Ådiameter. Comparing this to the predicted 131 Å-long AlphaFold2 models (Fig. 3.12 b), it can be concluded that the peripheral regions of LUBAC are missing in the reconstructed volumes. It could be excluded that the low resolution was due to incorrect training of crYOLO models, as both approaches led to similar results. To further

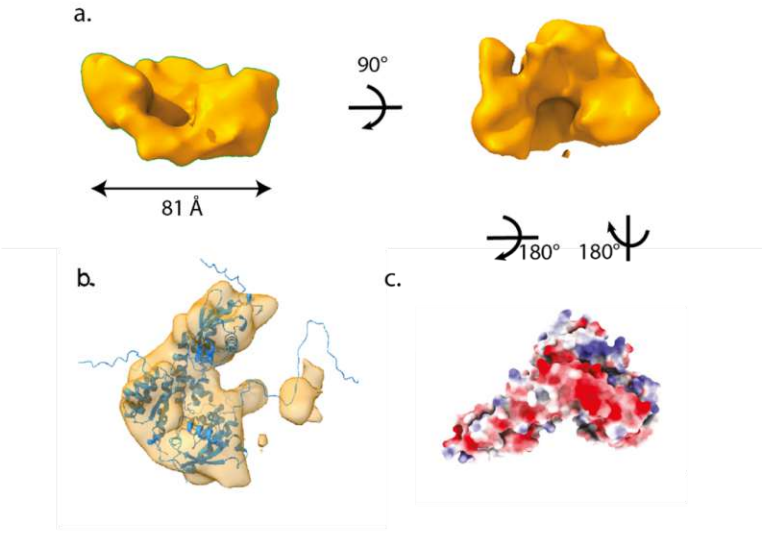

FIGURE 3.11: Reconstruction of LUBAC DCD. (a) cryoSPARC Ab Initio 1 model of LUBAC DCD (b) AlphaFold2 prediction of the trimeric core fitted into the Ab Initio 2. (c) Electric charge distribution of the trimeric core crystal structure (PDB:5Y3T). The AF2 prediction of the trimeric core is almost identical to the crystal structure (not shown).

investigate LUBAC, the viewing direction distribution was analysed and a preferred orientation of LUBAC at -pi/2 was found (Supp. Fig. 5.8 b). A highly negative charge at this orientation was observed by comparing the Ab Initio structures generated to the crystal structure of the trimeric core (Fig. 3.11 c). This observation strengthens the hypothesis that electrostatic forces could drive particles toward the air-water interface (AWI), which could cause the dissociation of LUBAC particles. Both, flexible regions of LUBAC and the dissociation of the AWI impede the proper representation of peripheral regions in the reconstructed maps. Potentially, optimization of the freezing procedure or grid preparation, in general, could facilitate the immersion of particles in ice (for example by time-resolved cryo-EM). This way, fewer dissociated particles would be included in the reconstruction procedure, and resolution could be increased.

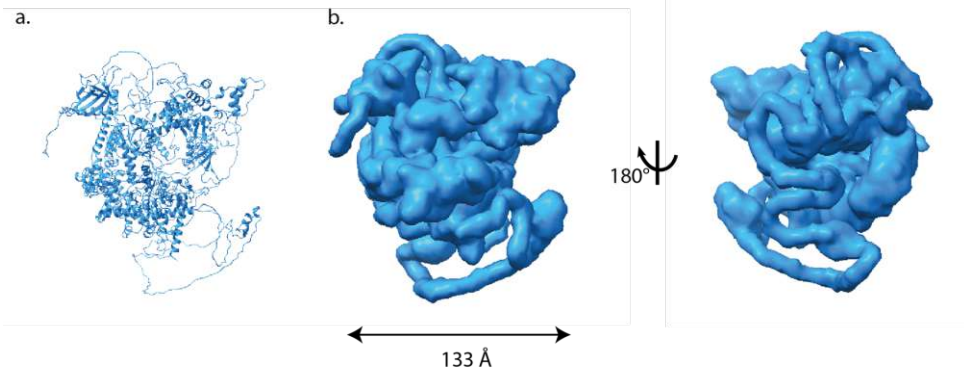

FIGURE 3.12: In Silico Reconstruction of full-length LUBAC obtained from Alphafold2. (a) Initial AF2 Model (b) Artificially generated model at 8 Åin ChimeraX.

Chapter 4

Discussion

In the attempt to structurally characterize the E3 ligase LUBAC, three variants were constructed for expression in insect cells and studied. Whilst all constructs were expressed, it was noted that protein yields, as well as sample quality, depended on the maintenance conditions of the insect cell cultures. Using culture volumes under 20% flask capacity allowed for higher viability and faster infection rates, most likely due to better aeration conditions. Higher volumes increased the required infection times and decreased the cell viability at the end of the infection. Optimising the SF9-cell-culture conditions is crucial regarding protein quality and is thus essential for all subsequent experiments. Addressing these issues and carefully preparing the insect cell culture has significantly improved LUBAC expression yields (Fig. 3.2). LUBAC constructs were purified using a two-step purification but co-purified with the contaminant ACC1. The purification protocol was revised as ACC1 had a similar molecular weight to LUBAC, which could interfere with MP and cryo-EM analyses. By introducing an on-column cleavage of the Strep-tagged LUBAC, the high-affinity binding ACC1 was captured by the Strep-resin and a pure LUBAC sample was obtained from the affinity column. The homogeneity and composition of the sample were verified by MP, which showed that the samples contain up to 90% of LUBAC monomers. Low amounts of HOIL-SHARPIN and LUBAC-dimers were detected (<20% for all samples, Supp. Fig. 5.1), but these were also further reduced by the aforementioned cell culture preparation optimization. Comparing the heterogeneity of LUBAC samples to previously published MP-data for similar protein complexes ([62] [27]), it can be concluded that the purity of the LUBAC sample presented in this work is very high. We observed that the purification of the LUBAC DCD construct had the highest yields and best stoichiometry (analysed by MP). As LUBAC DCD and LUBAC WT are most likely structurally identical, we mainly used LUBAC DCD for SPA. Additionally, ubiquitination experiments verified the functionality of the constructs in this thesis. The single point mutation C460A in HOIL-1L as well as C885A in HOIP (construct LUBAC DCD) completely inhibited the ubiquitination by LUBAC, in accordance with various other publications ([27], [76], [77]).

As the main aim of this thesis was to gain insights into the structure of the LUBAC complex, several grid preparation approaches were undertaken. LUBAC displayed good behaviour when negatively stained, showing intact protein complexes on grids. Several grid types were screened, and freezing LUBAC in Cu 200 mesh 1.2/1.3 grids showed the most promising particle behaviour. The particle quality could be improved by adding detergents (CHAPSO, Supp. Fig. 5.5) or grid-modification with PEI-GO (Fig. 3.9 c). Although the particles seemed to have better distribution across the grid holes and increased signal-to-noise ratio, they still dissociate. Therefore, we analysed and optimised the purification steps to increase protein quality. As a first step, we wanted to determine the ideal buffer conditions, which ProteoPlex could achieve. The experiments revealed that the optimal buffer conditions for LUBAC are in the higher pH spectrum (pH 8.0 – 9.0) for LUBAC. Therefore, these buffer conditions were used for all subsequent experiments

to ensure an optimal buffer environment for LUBAC. Because of this, it is rather unlikely that buffer or purification steps are the cause of insufficient particle quality in cryo-EM data collection. Furthermore, MP confirmed that the majority of proteins in the sample are indeed intact LUBAC complexes (Fig. 3.2). I also considered that LUBAC could dissociate because the affinity of its subunits is low. Binding LUBAC to one of its substrates or DUBs could stabilize the complex. In general, larger structures are easier to reconstruct and refine as they are easier to localize and align. Previous studies showed the deubiquitinating properties of OTULIN and its interaction with LUBAC subunit HOIP [34], [78]). Similarly, NEMO was found to be a target of M1-linear ubiquitination by LUBAC [79]. Both proteins were therefore promising candidates as potential binding partners of LUBAC in vitro. A high affinity/long-lasting interaction between these proteins and LUBAC was not observed. The most likely explanation for this is that the interaction of OTULIN-LUBAC and NEMO-LUBAC is transient. The short interaction times of E3 and their substrates are essential, as E3s need to ubiquitinate more than one substrate protein in a short period. Although this characteristic also applies to DUBs and their substrates, the interaction of HOIP and OTULIN was previously detected by SEC. However, only truncations of HOIP (PUB domain only) were used instead of the whole LUBAC construct [34]. Zinc-finger and RBR domains might influence the binding affinity of HOIP and OTULIN. The exclusion of these domains might have increased the affinity, as NZF and RBR domains might act as antagonists (also see introduction). Therefore, the binding affinity of LUBAC-OTULIN might be reduced compared to HOIP-OTULIN. Alternatively, the experiments could be repeated with full-length HOIP and OTULIN. This way, the binding affinity could be further analysed and evaluated. Lastly, it is worth mentioning that the AlphaFold2 prediction of the LUBAC structure shows that the PUB domain of HOIP is exposed on the surface of LUBAC. This suggests that the PUB domain is potentially available for interaction with other proteins.

For similar reasons as above, the interaction of UbCH7 and UbCH5b with LUBAC was investigated. HOIP with UbCH5b co-migrated on the gradient, pointing to a possible stable complex formation between the two. Indeed, MP data analysis further confirmed that HOIP-UbCH5b formed a stable complex. In contradiction to the findings of (Martino et al., 2018), no interaction of UbCH7 with neither LUBAC nor HOIP could be detected. However, in ubiquitination experiments (Fig. 3.7), using E2 UbCH7 was sufficient to ensure ubiquitination by LUBAC. It can be concluded that UbCH7 is associated with LUBAC with lower affinity and more transiently than UbCH5b. The gradient method was chosen due to the mild conditions for proteins and complexes and its ability to display the binding interaction of different proteins. Although the LUBAC sample used had high purity compared to other publications ([27], Fig. 3.2), full exclusion of other species such as SHARPIN-HOIL dimers, HOIP monomers and LUBAC dimers, is not very probable. Looking at the gradient gel, it appeared that UbCH5b was binding to the SHARPIN-HOIL dimer. However, MP data revealed that UbCH5b was interacting with HOIP. The interaction of UbcH5b with full LUBAC could not be proven in our gradients. From these results it is difficult to estimate an affinity between LUBAC and UbCH5b. On the one hand it is possible that HOIP monomers show a higher affinity for UbCH5b than LUBAC; on the other hand, it might be that UbCH5b-HOIP complex formation inhibits LUBAC assembly. As it was shown that HOIP alone is sufficient for linear Ub chain formation [31], it is possible that first the E2 bind HOIP to conjugate the Ub and then HOIL-SHARPIN are recruited to form the full LUBAC and expand or catalyse LUBACs function. The binding of UbCH5b to LUBAC could be elaborated in more detail by conducting additional immunoprecipitation or SEC experiments and comparing them to experiments shown in this thesis. Nevertheless, the main goal of increasing the size of LUBAC particles by attaching an E2 could be achieved neither by UbCH7 nor UbCH5b.

As all other efforts to increase particle quality did not lead to a high-resolution map of LUBAC, we initiated a detailed analysis of grid preparation. As stated before, changing neither grid type nor plunge freezing settings or using different detergents improved particle quality. I hypothesised that the plunge freezing technique itself might induce a hostile environment for proteins, during which the proteins are exposed to a high surface-to-volume ratio. Exposure to the air-water interface can cause partial or complete denaturation of the protein [80]. Even if the protein stays intact, adsorption to the air-water interface might induce preferential orientation ([81]). This reasoning is also in coherence with the observations made in Fig. 3.9 and Fig. 5.8. A preferred orientation at -pi/2 was displayed during homogeneous refinement in cryoSparc. Analysis of the electrostatic charges at this orientation revealed a highly negative and local charge. Although the electrostatic forces at the air-water interface are yet not fully understood, the local concentration of charges might facilitate the adsorption of regions to the interface. Cryo-ET allowed to localize particles to the upper meniscus, proving that LUBAC is indeed pushed towards the air-water interface. Approaches to reduce LUBAC adsorption to the air water interface were therefore sought after. Using PEI-GO grids, particles are concentrated in dry regions (Fig. 3.9 c). Although, the GO coating usually improves immersion of particles in ice it seemed that the adhesion of LUBAC for the AWI could not be fully eliminated. Possibly, LUBAC particles are pushed towards dry regions to minimize the exposure to the solution (position of least contact). Even though the addition of detergents (such as CHAPSO) improved the overall ice quality (Supp. Fig. 5.5), dissociation of LUBAC was still observed. As a next step, several approaches can be undertaken to improve the sample quality. First, as CHAPSO appeared to improve the ice and sample, other detergents, which have not been tested in this thesis, might show more optimal results. Time-resolved cryo-EM is another alternative approach. Due to the rapid (55 msec) freezing procedure, particles do not have enough time to adhere to the interface, effectively "trapping" the particles in solution [82].

Despite the challenges during grid preparation, this thesis obtained a low-resolution structure of the trimeric core, for which there is already a (high resolved) crystal structure. AlphaFold2 predictions for the structure of LUBAC displayed a high percentage of unstructured regions. This could mean that the flexibility of LUBAC gives only a limited imaging contrast, which could result in poorly resolved peripheral regions. Besides the "disassembling LUBAC" hypothesis, the internal flexibility of the subunits provides an alternative explanation for the obtained maps. Even if LUBAC is very flexible, different peripheral regions should be displayed partially in different datasets unless there is a preferential orientation due to the adsorption to the AWI or electrostatic forces. As the movement of domains is restrained by the geometrical assembly of the amino acids, volume densities should be visible, which is not the case for the datasets collected in this thesis. Reducing the threshold in maps only increased noise, while additional structure features did not emerge. I conclude that the adsorption to the air-water interface is the main cause of LUBAC dissociation. It is possible to argue that since the reconstructed Ab Initio map in this thesis is of low resolution, the structure of the trimeric core (PDB:5y3t) fits by chance. However, from the crystal structure of the trimeric core, it can be anticipated that the interaction of the UBA domain of HOIP and the UBL domains of HOIL-1L and SHARPIN is indeed present in the reconstructed LUBAC volume. Furthermore, as the trimeric core was successfully crystallized, this suggests that it is rigid, which can explain why only this region was successfully reconstructed.

4.1 Summary

This work showed that LUBAC could be purified from insect cells with a very high purity of the sample. Although the ideal conditions, such as buffer and pH, were analysed, only a low-resolution structure of the trimeric core was found. Further experiments need to be conducted to improve the immersion of particles in ice. Tomography experiments displayed the adsorption of particles to the air-water interface, which could be one of the reasons for LUBAC disassembly. Time-resolved methods should be considered in future, as their short plunging duration reduces the time during which particles can diffuse to the air-water interface. As LUBAC is the only E3 known to generate linear Ub chains, obtaining a high-resolution structure for LUBAC is crucial for understanding how M1-linked Ub chains are formed. Obtaining the structure can significantly aid in uncovering this poorly understood biochemical mechanism. Furthermore, the structure could bring new insights into the role of M1-linked chains in NF-kB signalling. The structure of LUBAC remains an essential milestone in describing these mechanisms. This thesis provided a basis for sample preparation for single-particle cryo-EM, which could guide future experiments to obtain the LUBAC structure.

Chapter 5

Supplementary Section

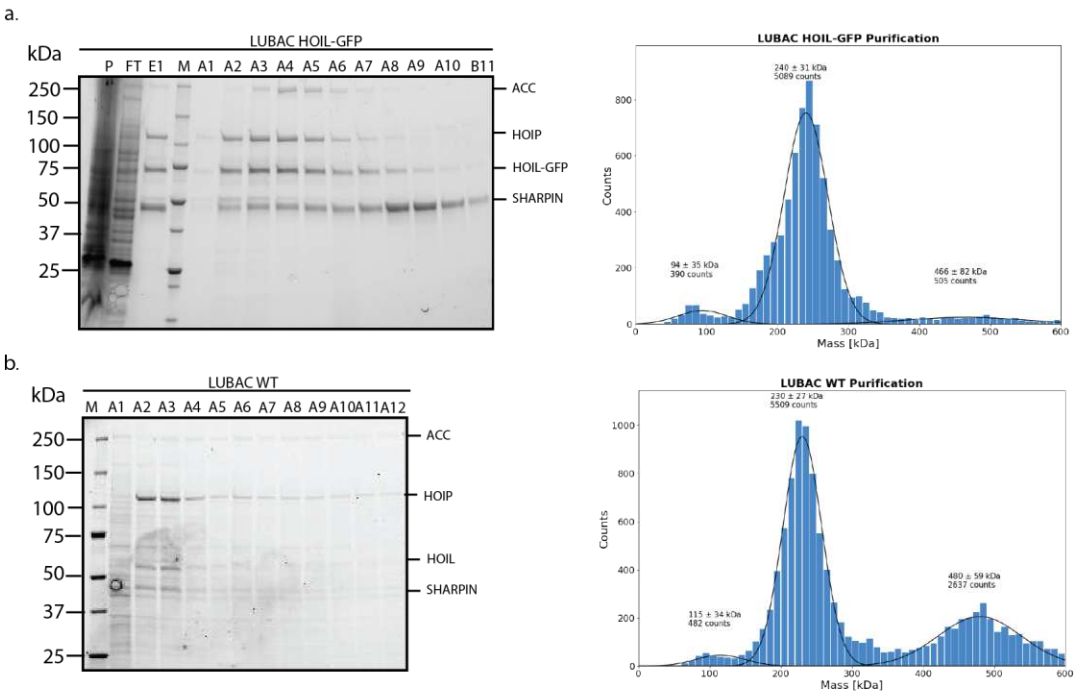

SUPPLEMENTARY FIGURE 5.1: Purification of LUBAC HOIL-GFP and LUBAC WT. (a) SDS-Page of LUBAC HOIL-GFP after SAC and SEC and MP measurement. LUBAC HOIL-GFP (249 kDa) peak contains almost 90% of all particles detected. b. SDS-Page of LUBAC WT after SAC and SEC and MP measurement. LUBAC WT (222 kDa) peak contains almost 65% of all particles detected and roughly 30% were LUBAC dimers (444 kDa).

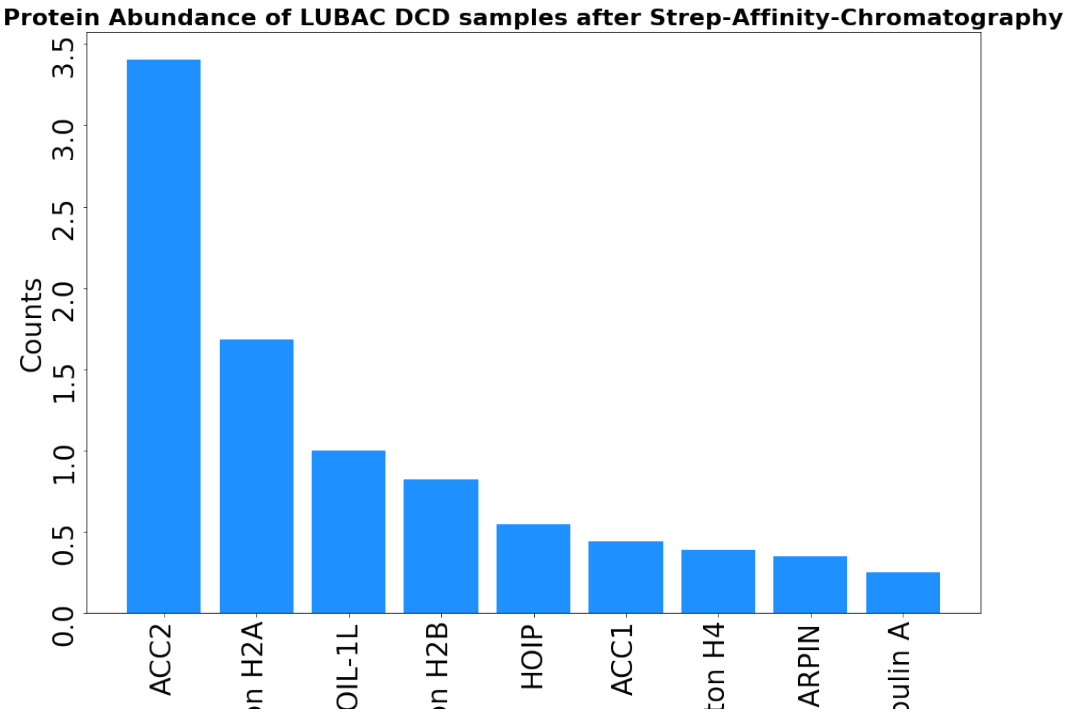

SUPPLEMENTARY FIGURE 5.2: Mass Spectrometry results showed a high abundance of ACC2 and ACC1. Data normalised to HOIL-1L

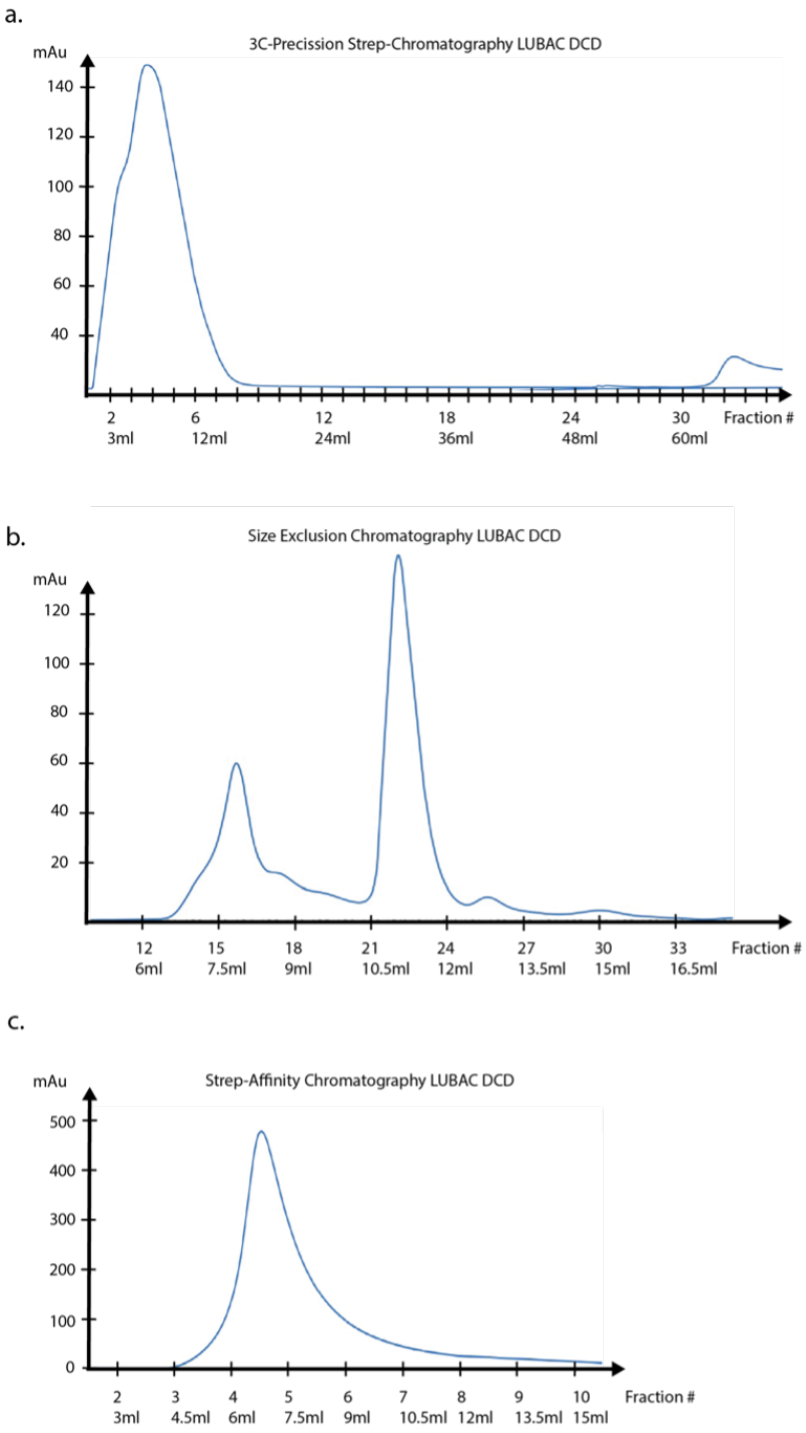

SUPPLEMENTARY FIGURE 5.3: Chromatography profiles of LUBAC DCD. (a) On column cleavage of the 3C-Strep-tag. 3C-Precission protease was injected into the loaded column and incubated overnight. LUBAC was eluted within the first 8 fractions while the ACC1 contaminant was eluted by GF-Buffer with Desthiobiotin in fractions C.6 and higher. Fraction size was 1.5 ml (b) SEC (Superdex 200 10/300GL column) with a fraction size of 0.5 ml. The first peak resembles full LUBAC constructs while the second peak only embodies HOIL-SHARPIN dimers mainly. (c) Chromatography profiles of LUBAC DCD. (a) Strep-affinity Chromatography (StrepTrap 5 ml column) of LUBAC with fraction size of 1.5 ml.

Pipetting Order	Component	Stock	LUBAC WT -ATP	LUBAC WT +ATP
1.	H2O		23.2 ul	15.2
2.	HEPES pH 8.0	500 mM	4.0	4.0
3.	NaCl	5 M	1.2	1.2
4.	MgSO4	10 mM	2.0	2.0
Mix by pipetting or gentle vortexing				
5.	Uba1	0.5 mg/ml	3.2	3.2
6.	UBCH7	0.1 mg/ml	2.4	2.4
7.	LUBAC	1.3 mg/ml	2.0	2.0
8.	Ubiquitin WT	10 mg/ml	1.0	1.0
9.	FL-Ub	10 mg/ml	1.0	1.0
Mix by pipetting or gentle vortexing				
10.	ATP	10 mM	0	8.0
Mix by pipetting or gentle vortexing				

TABLE 5.1: Ubiquitination assay protocol. The table shows pipetting order for ubiquitination experiments for LUBAC WT. The volumes of sample added were adjusted depending on the initial concentration of the sample for other constructs.

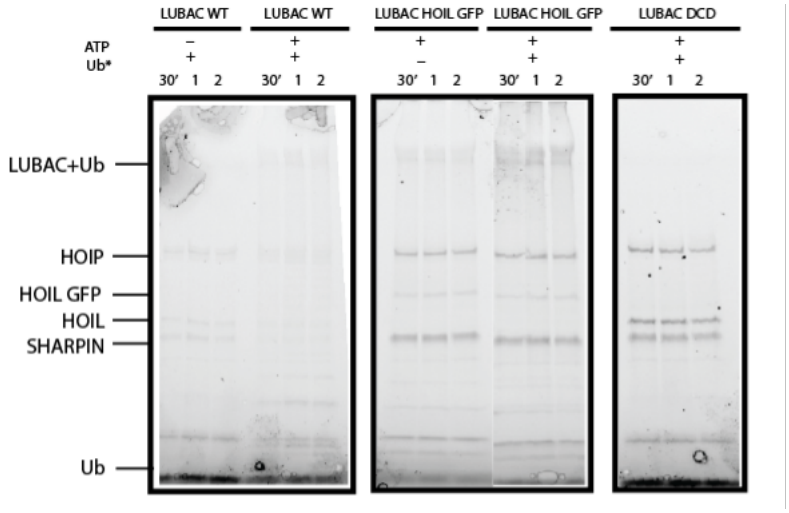

SUPPLEMENTARY FIGURE 5.4: Ubiquitination assay. The stain-free gel is presented to confirm the presence of all three LUBAC components.

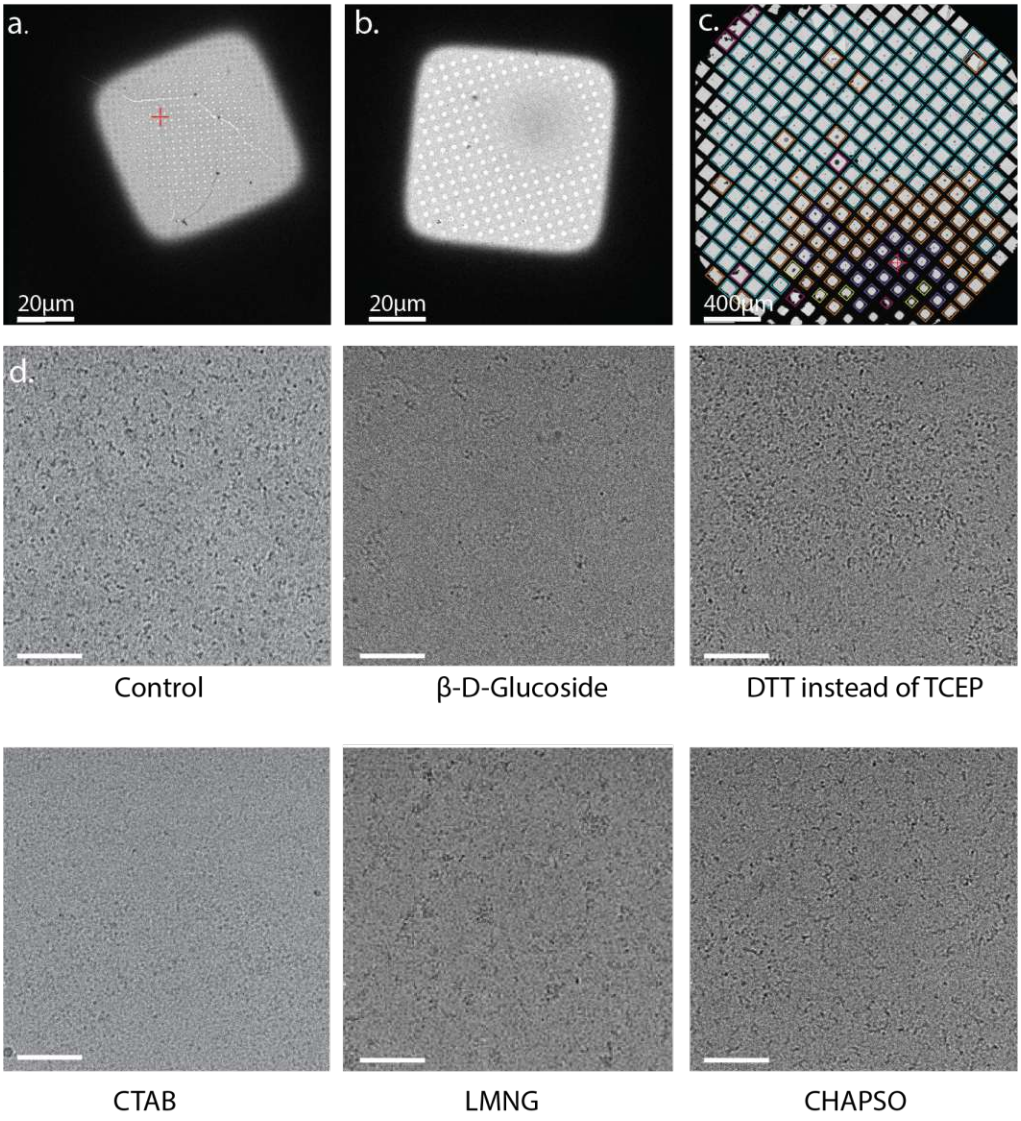

SUPPLEMENTARY FIGURE 5.5: Impact of detergents on particle distribution. (a) representative grid square for samples with no detergent. (b) grid square of sample modified with beta-D-Glucoside (c) map of unmodified sample (d) images in the centre of the grid hole for a sample without the addition of detergents, 0.05% beta-D-Glucoside, DTT instead of TCEP, 0.02% CTAB, 0.005% LMNG, 0.01% CHAPSO

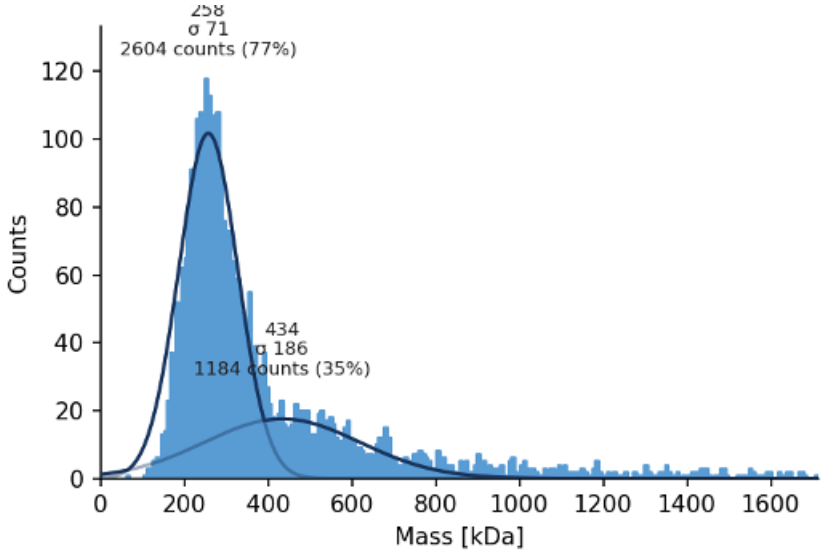

SUPPLEMENTARY FIGURE 5.6: MP measurement after SEC of LUBAC HOIL-GFP treated with PEG12. Histogram peaks appear to be broader compared to untreated samples. This is due to variations in PEG12 quantity that are bound to single proteins. Similarly, fractions on the gel are also spread for treated samples.

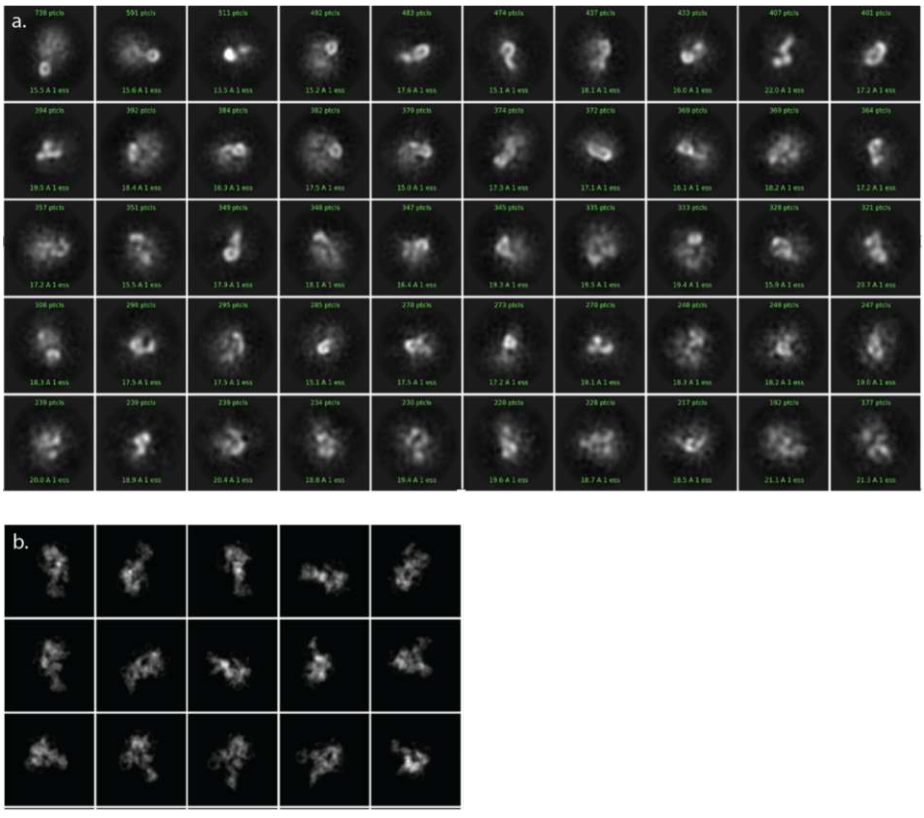

SUPPLEMENTARY FIGURE 5.7: 2D classification in cryoSparc. (a) 2D classification from recorded Dataset. Particles were picked with cryoYOLO with a training set of manually picked particles. (b) Templates generated in cryoSPARC. AlphaFold2 structure of LUBAC was converted into an artificial map with a resolution of 8 Åwith the ChimeraX command molMap (see Supp. Fig. 8)

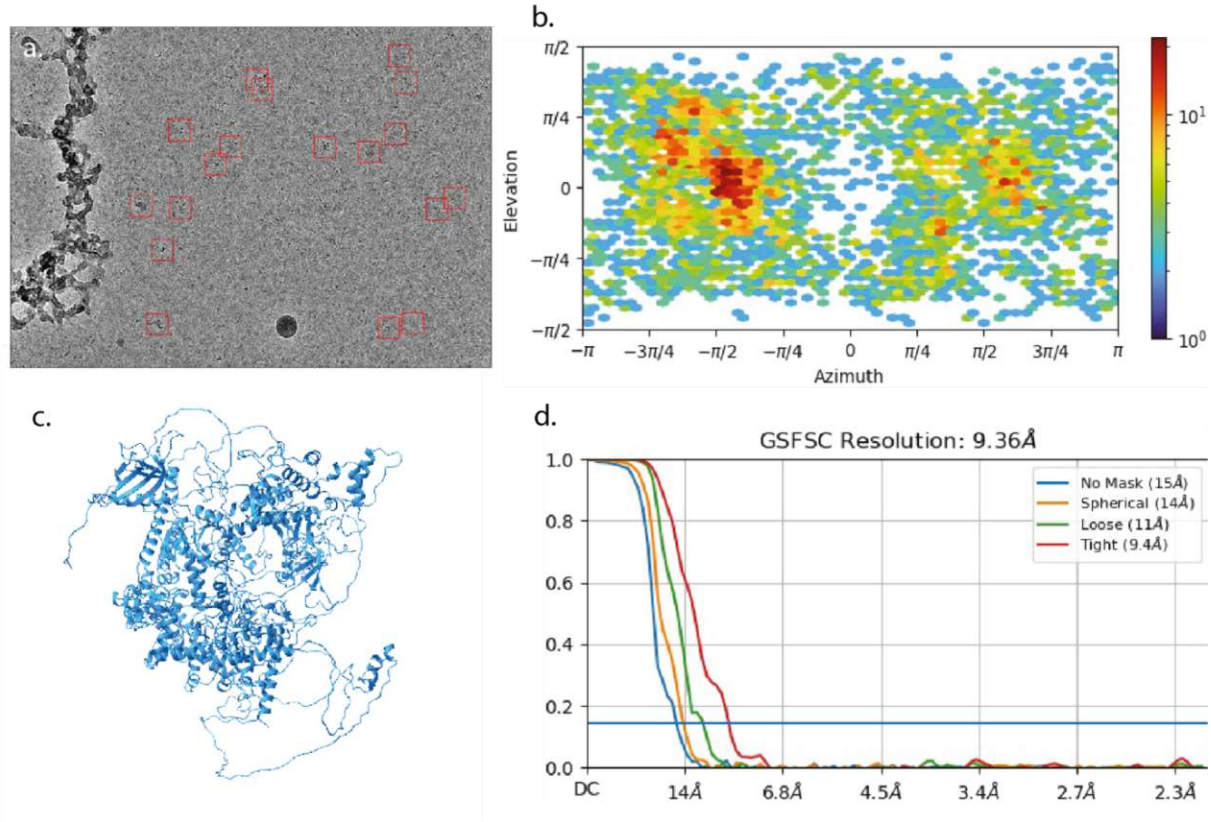

SUPPLEMENTARY FIGURE 5.8: Cryo-EM of LUBAC DCD. (a) Alphafold2 prediction of LUBAC and below generated map (8 Åresolution) with molMap command in ChimearX (b) view orientation distribution of Ab Initio model 1 reveals preferential orientation of LUBAC (c) FSC curve for Homogenous refinement shows the trimeric core was resolved to a resolution of 10 Å.

Bibliography

[1] G. A. Khoury, R. C. Baliban, and C. A. Floudas, "Proteome-wide post-translational modification statistics: Frequency analysis and curation of the swiss-prot database," *Scientific Reports*, vol. 1, 2011, ISSN: 20452322. DOI: 10.1038/srep00090.

[2] K. Kliza and K. Husnjak, "Resolving the complexity of ubiquitin networks," *Frontiers in Molecular Biosciences*, vol. 7, Feb. 2020, ISSN: 2296889X. DOI: 10.3389/fmolb.2020.00021.

[3] L. Randles and K. J. Walters, "Ubiquitin and its binding domains," vol. 17, pp. 2140–57, 2012. DOI: 10.2741/4042.

[4] Y. Inoue and T. Imamura, "Regulation of tgf- family signaling by e3 ubiquitin ligases," *Cancer Science*, vol. 99, pp. 2107–2112, 11 2008, ISSN: 13479032. DOI: 10.1111/j.1349-7006.2008.00925.x.

[5] K. I. Nakayama and K. Nakayama, "Ubiquitin ligases: Cell-cycle control and cancer," *Nature Reviews Cancer*, vol. 6, pp. 369–381, 5 May 2006, ISSN: 1474175X. DOI: 10.1038/nrc1881.

[6] C. Natarajan and K. Takeda, "Regulation of various dna repair pathways by e3 ubiquitin ligases," *Journal of Cancer Research and Therapeutics*, vol. 13, pp. 157–169, 2 Apr. 2017, ISSN: 19984138. DOI: 10.4103/0973-1482.204879.

[7] J. Callis, "The ubiquitination machinery of the ubiquitin system," *The Arabidopsis Book*, vol. 12, e0174, Jan. 2014, ISSN: 1543-8120. DOI: 10.1199/tab.0174.

[8] D. Rotin and S. Kumar, "Physiological functions of the hect family of ubiquitin ligases," *Nature Reviews Molecular Cell Biology*, vol. 10, pp. 398–409, 6 Jun. 2009, ISSN: 14710072. DOI: 10.1038/nrm2690.

[9] D. M. Wenzel, A. Lissounov, P. S. Brzovic, and R. E. Klevit, "Ubch7 reactivity profile reveals parkin and hhari to be ring/hect hybrids," *Nature*, vol. 474, pp. 105–108, 7349 Jun. 2011, ISSN: 00280836. DOI: 10.1038/nature09966.

[10] J. J. Smit and T. K. Sixma, "Rbr e3-ligases at work," *EMBO Reports*, vol. 15, pp. 142–154, 2 2014, ISSN: 14693178. DOI: 10.1002/embr.201338166.

[11] E. M. Well, V. Bader, M. Patra, *et al.*, "A protein quality control pathway regulated by linear ubiquitination," *The EMBO Journal*, vol. 38, 9 May 2019, ISSN: 0261-4189. DOI: 10.15252/embj.2018100730.

[12] M. E. French, C. F. Koehler, and T. Hunter, "Emerging functions of branched ubiquitin chains," *Cell Discovery*, vol. 7, 1 Dec. 2021, ISSN: 20565968. DOI: 10.1038/s41421-020-00237-y.

[13] B. A. Malynn and A. Ma, "Ubiquitin makes its mark on immune regulation," *Immunity*, vol. 33, pp. 843–852, 6 Dec. 2010, ISSN: 10747613. DOI: 10.1016/j.immuni.2010.12.007.

[14] A. D. Jacobson, N. Y. Zhang, P. Xu, *et al.*, "The lysine 48 and lysine 63 ubiquitin conjugates are processed differently by the 26 s proteasome," *Journal of Biological Chemistry*, vol. 284, pp. 35 485–35 494, 51 Dec. 2009, ISSN: 00219258. DOI: 10.1074/jbc.M109.052928.

[15] E. S. Johnson, P. C. Ma, I. M. Ota, and A. Varshavsky, "A proteolytic pathway that recognizes ubiquitin as a degradation signal," *Journal of Biological Chemistry*, vol. 270, pp. 17 442–17 456, 29 1995, ISSN: 00219258. DOI: 10.1074/jbc.270.29.17442.

[16] H. J. Meyer and M. Rape, "Enhanced protein degradation by branched ubiquitin chains," *Cell*, vol. 157, pp. 910–921, 4 May 2014, ISSN: 10974172. DOI: 10.1016/j.cell.2014.03.037.

[17] B. Stieglitz, A. C. Morris-Davies, M. G. Koliopoulos, E. Christodoulou, and K. Rittinger, "Lubac synthesizes linear ubiquitin chains via a thioester intermediate," *EMBO Reports*, vol. 13, pp. 840–846, 9 Sep. 2012, ISSN: 1469221X. DOI: 10.1038/embor.2012.105.

[18] B. C. Lechtenberg, A. Rajput, R. Sanishvili, *et al.*, "Structure of a hoip/e2ubiquitin complex reveals rbr e3 ligase mechanism and regulation," *Nature*, vol. 529, pp. 546–550, 7587 Jan. 2016, ISSN: 14764687. DOI: 10.1038/nature16511.

[19] M. S. Hayden and S. Ghosh, "Regulation of nf-b by tnf family cytokines," *Seminars in Immunology*, vol. 26, pp. 253–266, 3 2014, ISSN: 10963618. DOI: 10.1016/j.smim.2014.05.004.

[20] G. Middleton, M. Hamanoue, Y. Enokido, *et al.*, "Cytokine-induced nuclear factor kappa b activation promotes the survival of developing neurons," 2000, pp. 325–332. [Online]. Available: http://www.jcb.org.

[21] H. Oh and S. Ghosh, "Nf-b: Roles and regulation in different cd4+ t-cell subsets," *Immunological Reviews*, vol. 252, pp. 41–51, 1 Mar. 2013, ISSN: 01052896. DOI: 10.1111/imr.12033.

[22] T. Lawrence, "The nuclear factor nf-kappab pathway in inflammation.," *Cold Spring Harbor perspectives in biology*, vol. 1, 6 2009, ISSN: 19430264. DOI: 10.1101/cshperspect.a001651.

[23] S. Beinke and S. C. Ley, "Functions of nf-b1 and nf-b2 in immune cell biology," 2004, pp. 393–409.

[24] T. L. Haas, C. H. Emmerich, B. Gerlach, *et al.*, "Recruitment of the linear ubiquitin chain assembly complex stabilizes the tnf-r1 signaling complex and is required for tnf-mediated gene induction," *Molecular Cell*, vol. 36, pp. 831–844, 5 Dec. 2009, ISSN: 10972765. DOI: 10.1016/j.molcel.2009.10.013.

[25] A. R. Brasier, "The nuclear factor-b-interleukin-6 signalling pathway mediating vascular inflammation," *Cardiovascular Research*, vol. 86, pp. 211–218, 2 May 2010, ISSN: 00086363. DOI: 10.1093/cvr/cvq076.

[26] J. W. Lim, H. Kim, and K. H. Kim, "Nuclear factor-b regulates cyclooxygenase-2 expression and cell proliferation in human gastric cancer cells," 2001.

[27] A. R. Carvajal, I. Grishkovskaya, C. G. Diaz, *et al.*, "The linear ubiquitin chain assembly complex (lubac) generates heterotypic ubiquitin chains," *eLife*, vol. 10, Jun. 2021, ISSN: 2050084X. DOI: 10.7554/eLife.60660.

[28] H. Yagi, K. Ishimoto, T. Hiromoto, *et al.*, "A non-canonical uba-ubl interaction forms the linear-ubiquitin-chain assembly complex," *EMBO Reports*, vol. 13, pp. 462–468, 5 May 2012, ISSN: 1469221X. DOI: 10.1038/embor.2012.24.

[29] B. Gerlach, S. M. Cordier, A. C. Schmukle, *et al.*, "Linear ubiquitination prevents inflammation and regulates immune signalling," *Nature*, vol. 471, pp. 591–596, 7340 Mar. 2011, ISSN: 00280836. DOI: 10.1038/nature09816.

[30] I. R. Kelsall, J. Zhang, A. Knebel, S. J. Arthur, and P. Cohen, "The e3 ligase hoil-1 catalyses ester bond formation between ubiquitin and components of the myddosome in mammalian cells," *Proceedings of the National Academy of Sciences of the United States of America*, vol. 116, pp. 13 293–13 298, 27 2019, ISSN: 10916490. DOI: 10.1073/pnas.1905873116.

[31] J. J. Smit, D. Monteferrario, S. M. Noordermeer, W. J. V. Dijk, B. A. V. D. Reijden, and T. K. Sixma, "The e3 ligase hoip specifies linear ubiquitin chain assembly through its ring-ibr-ring domain and the unique ldd extension," *EMBO Journal*, vol. 31, pp. 3833–3844, 19 Oct. 2012, ISSN: 02614189. DOI: 10.1038/emboj.2012.217.

[32] B. Boisson, E. Laplantine, C. Prando, *et al.*, "Immunodeficiency, autoinflammation and amylopectinosis in humans with inherited hoil-1 and lubac deficiency," *Nature Immunology*, vol. 13, pp. 1178–1186, 12 Dec. 2012, ISSN: 15292908. DOI: 10.1038/ni.2457.

[33] J. Zinngrebe, E. Rieser, L. Taraborrelli, *et al.*, "Lubac deficiency perturbs tlr3 signaling to cause immunodeficiency and autoinflammation," *Journal of Experimental Medicine*, vol. 213, pp. 2671–2689, 12 Nov. 2016, ISSN: 15409538. DOI: 10.1084/jem.20160041.

[34] P. R. Elliott, S. V. Nielsen, P. Marco-Casanova, *et al.*, "Molecular basis and regulation of otulin-lubac interaction," *Molecular Cell*, vol. 54, pp. 335–348, 3 May 2014, ISSN: 10974164. DOI: 10.1016/j.molcel.2014.03.018.

[35] B. K. Fiil, R. B. Damgaard, S. A. Wagner, *et al.*, "Otulin restricts met1-linked ubiquitination to control innate immune signaling," *Molecular Cell*, vol. 50, pp. 818–830, 6 Jun. 2013, ISSN: 10972765. DOI: 10.1016/j.molcel.2013.06.004.

[36] K. Keusekotten, P. R. Elliott, L. Glockner, *et al.*, "Xotulin antagonizes lubac signaling by specifically hydrolyzing met1-linked polyubiquitin," *Cell*, vol. 153, p. 1312, 6 Jun. 2013, ISSN: 10974172. DOI: 10.1016/j.cell.2013.05.014.

[37] B. K. Fiil and M. Gyrd-Hansen, "Otulin deficiency causes auto-inflammatory syndrome," *Cell Research*, vol. 26, pp. 1176–1177, 11 Nov. 2016, ISSN: 17487838. DOI: 10.1038/cr.2016.113.

[38] H. Verschueren, "Interference reflection microscopy in cell biology: Methodology and applications," 1985, pp. 279–301.

[39] J. O. Arroyo, D. Cole, and P. Kukura, "Interferometric scattering microscopy and its combination with single-molecule fluorescence imaging," *Nature Protocols*, vol. 11, pp. 617–633, 4 Apr. 2016, ISSN: 17502799. DOI: 10.1038/nprot.2016.022.

[40] F. Soltermann, E. D. Foley, V. Pagnoni, *et al.*, "Quantifying protein–protein interactions by molecular counting with mass photometry," *Angewandte Chemie - International Edition*, vol. 59, pp. 10 774–10 779, 27 Jun. 2020, ISSN: 15213773. DOI: 10.1002/anie.202001578.

[41] L. E. Franken, K. Grünewald, E. J. Boekema, and M. C. Stuart, "A technical introduction to transmission electron microscopy for soft-matter: Imaging, possibilities, choices, and technical developments," *Small*, vol. 16, 14 Apr. 2020, ISSN: 16136829. DOI: 10.1002/smll.201906198.

[42] K. M. Yip, N. Fischer, E. Paknia, A. Chari, and H. Stark, "Atomic-resolution protein structure determination by cryo-em," *Nature*, vol. 587, pp. 157–161, 7832 Nov. 2020, ISSN: 14764687. DOI: 10.1038/s41586-020-2833-4.

[43] M. Adrian, J. Dubochet, J. Lepault, and A. W. McDowall, "Cryo-electron microscopy of viruses," *Nature*, vol. 308, pp. 32–36, 5954 Mar. 1984, ISSN: 0028-0836. DOI: 10.1038/308032a0. [Online]. Available: http://www.nature.com/articles/308032a0.

[44] H. W. Wang and J. W. Wang, "How cryo-electron microscopy and x-ray crystallography complement each other," *Protein Science*, vol. 26, pp. 32–39, 1 Jan. 2017, ISSN: 1469896X. DOI: 10.1002/pro.3022.

[45] M. Wu and G. C. Lander, "How low can we go? structure determination of small biological complexes using single-particle cryo-em," *Current Opinion in Structural Biology*, vol. 64, pp. 9–16, Oct. 2020, ISSN: 1879033X. DOI: 10.1016/j.sbi.2020.05.007.

[46] L. E. Franken, K. Grünewald, E. J. Boekema, and M. C. Stuart, "A technical introduction to transmission electron microscopy for soft-matter: Imaging, possibilities, choices, and technical developments," *Small*, vol. 16, 14 Apr. 2020, ISSN: 16136829. DOI: 10.1002/smll.201906198.

[47] R. A. Grassucci, D. J. Taylor, and J. Frank, "Preparation of macromolecular complexes for cryo-electron microscopy," *Nature Protocols*, vol. 2, pp. 3239–3246, 12 Dec. 2007, ISSN: 17502799. DOI: 10.1038/nprot.2007.452.

[48] D. P. Klebl, M. S. Gravett, D. Kontziampasis, *et al.*, "Need for speed: Examining protein behavior during cryoem grid preparation at different timescales," *Structure*, vol. 28, 1238–1248.e4, 11 Nov. 2020, ISSN: 18784186. DOI: 10.1016/j.str.2020.07.018.

[49] J. R. Gallagher, A. J. Kim, N. M. Gulati, and A. K. Harris, "Negative-stain transmission electron microscopy of molecular complexes for image analysis by 2d class averaging," *Current Protocols in Microbiology*, vol. 54, 1 Sep. 2019, ISSN: 19348533. DOI: 10.1002/cpmc.90.

[50] M. Hohn, G. Tang, G. Goodyear, *et al.*, "Sparx, a new environment for cryo-em image processing," *Journal of Structural Biology*, vol. 157, pp. 47–55, 1 Jan. 2007, ISSN: 10478477. DOI: 10.1016/j.jsb.2006.07.003.

[51] A. Punjani, J. L. Rubinstein, D. J. Fleet, and M. A. Brubaker, "Cryosparc: Algorithms for rapid unsupervised cryo-em structure determination," *Nature Methods*, vol. 14, pp. 290–296, 3 Feb. 2017, ISSN: 15487105. DOI: 10.1038/nmeth.4169.

[52] S. H. Scheres, "Relion: Implementation of a bayesian approach to cryo-em structure determination," *Journal of Structural Biology*, vol. 180, pp. 519–530, 3 Dec. 2012, ISSN: 10478477. DOI: 10.1016/j.jsb.2012.09.006.

[53] A. B. Nowakowski, W. J. Wobig, and D. H. Petering, "Native SDS-PAGE: High Resolution Electrophoretic Separation of Proteins With Retention of Native Properties Including Bound Metal Ions," *Metallomics : integrated biometal science*, vol. 6, no. 5, pp. 1068–1078, May 2014, ISSN: 1756-5901. DOI: 10.1039/c4mt00033a. [Online]. Available: https://www.ncbi.nlm.nih.gov/pmc/articles/PMC4517606/ (visited on 03/25/2022).

[54] C. J. V. Wintersdorff, J. Penders, J. M. V. Niekerk, *et al.*, "Dissemination of antimicrobial resistance in microbial ecosystems through horizontal gene transfer," *Frontiers in Microbiology*, vol. 7, FEB Feb. 2016, ISSN: 1664302X. DOI: 10.3389/fmicb.2016.00173.

[55] A. Froger and J. E. Hall, "Transformation of plasmid dna into e. coli using the heat shock method," *Journal of Visualized Experiments*, 6 Jul. 2007, ISSN: 1940087X. DOI: 10.3791/253.

[56] I. Iost, J. Guillerez, and M. Dreyfus, "Notes bacteriophage t7 rna polymerase travels far ahead of ribosomes in vivo," 1992, pp. 619–622. [Online]. Available: https://journals.asm.org/journal/jb.

[57] A. H. E. C. M. L. P. J. V. C. Brian Dalbya Sharon Catesa, "Advanced transfection with lipofectamine 2000 reagent: Primary neurons, sirna, and high-throughput applications," *Elsevier*, vol. 33, pp. 95–103, 2 Jun. 2004, ISSN: 10974164. DOI: 10.1016/j.ymeth.2003.11.023.

[58] I. life technologies, "Guide to baculovirus expression vector systems (bevs) and insect cell culture techniques,"

[59] T. G. Schmidt and A. Skerra, "The strep-tag system for one-step purification and high-affinity detection or capturing of proteins," *Nature Protocols*, vol. 2, pp. 1528–1535, 6 Jun. 2007, ISSN: 17542189. DOI: 10.1038/nprot.2007.209.

[60] W. Hirst and R. A. Cox, "The construction and analysis of sucrose gradients for use with zonal rotors," 1976, pp. 259–265.

[61] W. M. et al., "Protein identification and analysis tools in the expasy server," *2-D Proteome Analysis Protocols. Methods in Molecular Biology*, vol. 112, pp. 531–552, 1999.

[62] A. Sonn-Segev, K. Belacic, T. Bodrug, *et al.*, "Quantifying the heterogeneity of macromolecular machines by mass photometry," *Nature Communications*, vol. 11, 1 Dec. 2020, ISSN: 20411723. DOI: 10.1038/s41467-020-15642-w.

[63] A. Chari, D. Haselbach, J. M. Kirves, *et al.*, "Proteoplex: Stability optimization of macromolecular complexes by sparse-matrix screening of chemical space," *Nature Methods*, vol. 12, pp. 859–865, 9 Aug. 2015, ISSN: 15487105. DOI: 10.1038/nmeth.3493.

[64] B. S and H. RW, "A negative staining method for high resolution electron microscopy of viruses," *Biochim Biophys Acta.*, vol. 34, Jul. 1959.

[65] R. F. Thompson, M. Walker, C. A. Siebert, S. P. Muench, and N. A. Ranson, "An introduction to sample preparation and imaging by cryo-electron microscopy for structural biology," *Methods*, vol. 100, pp. 3–15, May 2016, ISSN: 10959130. DOI: 10.1016/j.ymeth.2016.02.017.

[66] M. J. Dobro, L. A. Melanson, G. J. Jensen, and A. W. McDowall, "Plunge freezing for electron cryomicroscopy," *Methods in Enzymology*, vol. 481, pp. 63–82, C 2010, ISSN: 00766879. DOI: 10.1016/S0076-6879(10)81003-1.

[67] R. S. Pantelic, J. C. Meyer, U. Kaiser, W. Baumeister, and J. M. Plitzko, "Graphene oxide: A substrate for optimizing preparations of frozen-hydrated samples," *Journal of Structural Biology*, vol. 170, pp. 152–156, 1 Apr. 2010, ISSN: 10478477. DOI: 10.1016/j.jsb.2009.12.020.

[68] A. Patel, D. Toso, A. Litvak, and E. Nogales, "Efficient graphene oxide coating improves cryo-em sample preparation and data collection from tilted grids," DOI: 10.1101/2021.03.08.434344. [Online]. Available: https://doi.org/10.1101/2021.03.08.434344.

[69] J. R. Kremer, D. N. Mastronarde, and J. R. Mcintosh, "Computer visualization of three-dimensional image data using imod," 1996.

[70] T. Wagner, F. Merino, M. Stabrin, *et al.*, "Sphire-cryolo is a fast and accurate fully automated particle picker for cryo-em," *Communications Biology*, vol. 2, 1 Dec. 2019, ISSN: 23993642. DOI: 10.1038/s42003-019-0437-z.

[71] ——, "Sphire-cryolo is a fast and accurate fully automated particle picker for cryo-em," *Communications Biology*, vol. 2, 1 Dec. 2019, ISSN: 23993642. DOI: 10.1038/s42003-019-0437-z.

[72] J. Jumper, R. Evans, A. Pritzel, *et al.*, "Highly accurate protein structure prediction with alphafold," *Nature*, vol. 596, pp. 583–589, 7873 Aug. 2021, ISSN: 14764687. DOI: 10.1038/s41586-021-03819-2.

[73] T. D. Goddard, C. C. Huang, E. C. Meng, *et al.*, "Ucsf chimerax: Meeting modern challenges in visualization and analysis," *Protein Science*, vol. 27, pp. 14–25, 1 Jan. 2018, ISSN: 1469896X. DOI: 10.1002/pro.3235.

[74] V. Schaeffer, M. Akutsu, M. H. Olma, L. C. Gomes, M. Kawasaki, and I. Dikic, "Binding of otulin to the pub domain of hoip controls nf-b signaling," *Molecular Cell*, vol. 54, pp. 349–361, 3 May 2014, ISSN: 10974164. DOI: 10.1016/j.molcel.2014.03.016.

[75] Z. Zhang, H. Shigematsu, T. Shimizu, and U. Ohto, "Improving particle quality in cryo-em analysis using a pegylation method," *Structure*, vol. 29, 1192–1199.e4, 10 Oct. 2021, ISSN: 18784186. DOI: 10.1016/j.str.2021.05.004.

[76] L. M. Fennell, C. G. Diaz, L. Deszcz, *et al.*, "Site-specific ubiquitination of the e3 ligase hoip regulates apoptosis and immune signaling," *The EMBO Journal*, vol. 39, 24 Dec. 2020, ISSN: 0261-4189. DOI: 10.15252/embj.2019103303.

[77] L. Elton, I. Carpentier, J. Staal, Y. Driege, M. Haegman, and R. Beyaert, "Malt1 cleaves the e3 ubiquitin ligase hoil-1 in activated t cells, generating a dominant negative inhibitor of lubac-induced nf-b signaling," *FEBS Journal*, vol. 283, pp. 403–412, 3 Feb. 2016, ISSN: 17424658. DOI: 10.1111/febs.13597.

[78] K. Heger, K. E. Wickliffe, A. Ndoja, *et al.*, "Otulin limits cell death and inflammation by deubiquitinating lubac," *Nature*, vol. 559, pp. 120–124, 7712 Jul. 2018, ISSN: 14764687. DOI: 10.1038/s41586-018-0256-2.

[79] J. J. Smit, W. J. V. Dijk, D. E. Atmioui, R. Merkx, H. Ovaa, and T. K. Sixma, "Target specificity of the e3 ligase lubac for ubiquitin and nemo relies on different minimal requirements," *Journal of Biological Chemistry*, vol. 288, pp. 31 728–31 737, 44 Nov. 2013, ISSN: 00219258. DOI: 10.1074/jbc.M113.495846.

[80] H. B. Bull, "Spread monolayers of protein,"

[81] A. J. Noble, V. P. Dandey, H. Wei, *et al.*, "Routine single particle cryoem sample and grid characterization by tomography," 2018. DOI: 10.7554/eLife.34257.001. [Online]. Available: https://doi.org/10.7554/eLife.34257.001.

[82] V. P. Dandey, W. C. Budell, H. Wei, *et al.*, "Time-resolved cryoem using spotiton 1 2," DOI: 10.1101/2020.04.20.050518. [Online]. Available: https://doi.org/10.1101/2020.04.20.050518.